nature communications

Article

https://doi.org/10.1038/s41467-025-59725-y

# Streamlined metal-based hydrogel facilitates stem cell differentiation, extracellular matrix homeostasis and cartilage repair in male rats

Received: 22 November 2023

Accepted: 2 May 2025

Published online: 10 May 2025

Check for updates

Wen Li[1], Zhiyuan Shi[1], Huaqing Jing[1], Yunsheng Dou[1], Xinyi Liu[1], Mengyao Zhang[1], Zitong Qiu[1], Zbynek Heger[2] & Nan Li[1]

Dysregulation of extracellular matrix (ECM) homeostasis plays a pivotal role in the accelerated degradation of cartilage, presenting a notable challenge for effective osteoarthritis (OA) treatment and cartilage regeneration. In this study, we introduced an injectable hydrogel based on streamlined-zinc oxide (ZnO), which is responsive to matrix metallopeptidase (MMP), for the delivery of miR-17-5p. This approach aimed to address cartilage damage by regulating ECM homeostasis. The ZnO/miR-17-5p composite functions by releasing zinc ions to attract native bone marrow mesenchymal stem cells, thereby fostering ECM synthesis through the proliferation of new chondrocytes. Concurrently, sustained delivery of miR-17-5p targets enzymes responsible for matrix degradation, thereby mitigating the catabolic process. Notably, the unique structure of the streamlined ZnO nanoparticles is distinct from their conventional spherical counterparts, which not only optimizes the rheological and mechanical properties of the hydrogels, but also enhances the efficiency of miR-17-5p transfection. Our male rat model demonstrated that the combination of streamlined ZnO, MMP-responsive hydrogels, and miRNA-based therapy effectively managed the equilibrium between catabolism and anabolism within the ECM, presenting a fresh perspective in the realm of OA treatment.

Osteoarthritis (OA), acknowledged as the foremost chronic disabling ailment worldwide, is the most prevalent form of Arthritis[1,2]. The principal pathological hallmark revolves around degenerative changes in the articular cartilage[3]. The inherently limited self-repair capability of cartilage, rooted in the absence of vascular and neural networks, constitutes a fundamental barrier to curing OA[4,5]. Current treatment modalities, such as intra-articular injections and microfracture surgery, fail to ameliorate symptoms and enhance joint functionality owing to their inability to effectively restore the structure and biological function of the articular cartilage[6,7]. The extracellular matrix (ECM) contributes to approximately 90% of the dry weight of cartilage[8], playing a crucial role in the biomechanical properties of articular cartilage. Under normal physiological conditions, the ECM maintains a delicate equilibrium between anabolism and catabolism, which is crucial for maintaining the stability and structural integrity of cartilage. However, the progression of OA leads to the prevalence of catabolism over anabolism[9]. This imbalance disrupts ECM homeostasis and accelerates cartilage degeneration. Therefore, modulation of anabolism and catabolism to restore cartilage ECM homeostasis is a promising fundamental strategy against OA.

Chondrocytes, the sole cell type present in cartilage, play a vital role in ECM synthesis and renewal, thereby maintaining matrix balance and integrity[10]. Overcoming progressive cartilage breakdown in OA necessitates the recruitment of bone marrow mesenchymal stem cells (BMSCs) and their subsequent differentiation into new chondrocytes[11–13]. Extensive studies have demonstrated the importance of various growth factors, including transforming growth factor-β (TGF-β), in regulating stem cell growth, differentiation, and immune

[1]Tianjin Key Laboratory of Drug Delivery & High-Efficiency, School of Pharmaceutical Science and Technology, Faculty of Medicine, Tianjin University, Tianjin 300072, China. [2]Department of Chemistry and Biochemistry, Mendel University in Brno, Brno 613 00, Czech Republic. e-mail: linan1985@tju.edu.cn

function[14–16]. However, the practical application of these growth factors is hindered by challenges, such as poor retention at the defect site, instability, immunogenicity, and high cost[17]. Remarkably, zinc ions ($Zn^{2+}$) serve as crucial cofactors for numerous enzymes involved in DNA synthesis, immune function, and bone metabolism, such as alkaline phosphatase and collagenase[18–21]. Therefore, harnessing metal ions to promote anabolism is a promising strategy for rebalancing ECM homeostasis. Zinc oxide (ZnO) nanoparticles, known for their excellent biocompatibility and antibacterial properties, have been incorporated into bioceramics, such as tricalcium phosphate (TCP) and bioglass (BG) to optimize their mechanical properties and promote osteoblast/bone growth[22,23]. However, studies investigating the effects of ZnO NPs on cartilage regeneration are scarce.

Advances in the understanding of the pathogenesis of OA have spurred the exploration of therapeutic strategies targeting ECM catabolic processes[24]. Different strategies aim to combat OA by inhibiting the ECM components that contribute to cartilage degradation. For example, ligustilide inhibits the breakdown of ECM components by downregulating the expression of matrix metalloproteinases and chondroproteoglycan antibodies[25]. Contrary to traditional small molecules and antibody agents, RNA drugs offer unique advantages by exerting regulatory effects directly at the gene level, enabling targeted modulation of specific pathogenic genes[26]. Among these RNA drugs, miR-17-5p (miR-17), a member of the mir-17–92 cluster[27], has recently shown promise in combating ECM degradation. This is achieved by targeting key pathological catabolic factors, such as matrix metallopeptidase 13 (MMP13) and aggrecanase-2 (ADAMTS5), while suppressing a diverse range of matrix-degrading enzymes[28]. Therefore, the efficient delivery of miR-17 to chondrocytes exerts an inhibitory effect on ECM catabolism, potentially contributing to the amelioration of OA progression.

In this work, we propose an approach involving the co-delivery of miR-17 and streamlined ZnO to cartilage defects to modulate the balance between anabolism and catabolism for cartilage ECM homeostasis (Fig. 1). Our delivery system, GelMA/str-ZnO@PEI/miR-17 (str-ZPM Gel), mimics several biological and physical properties of the natural ECM, promoting cell proliferation, migration, and adhesion, while demonstrating good biocompatibility and biodegradability[29]. The distinctive streamlined structure of ZnO enhances the fluidity and mechanical properties of the GelMA hydrogel. Upon in situ injection, the str-ZPM Gel undergoes sustained release through progressive degradation, subsequently being internalized by the BMSCs and chondrocytes. Degradation of the str-ZPM Gel leads to the release of $Zn^{2+}$ ions, enhancing activation of the Ihh/PTHrP pathway. This, in turn, facilitates the recruitment and chondrogenic differentiation of BMSCs in vivo, resulting in an increased quantity of fresh chondrocytes and the promotion of ECM anabolism. Simultaneously, sustained delivery of miR-17 targets pathological catabolic factors, including MMP13 and ADAMTS5, thereby ameliorating persistent destruction of the cartilage ECM by inhibiting catabolism. Collectively, our study demonstrates that str-ZPM Gel effectively restores cartilage ECM homeostasis, providing protection to the cartilage and reinstating articular function. This approach offers a promising avenue for the treatment of cartilage degeneration in patients with OA.

## Results

### Preparation and characterization of str-ZnO NPs and str-ZPM Gel

In this study, we synthesized streamlined-ZnO (str-ZnO) nanoparticles loaded with polyethyleneimine (PEI) and miR-17, which were embedded in methacrylated gelatin (GelMA) composite hydrogels (Fig. 2a). Str-ZnO NPs were prepared via non-aqueous ammonolysis using anhydrous zinc acetate as the raw material (Supplementary Fig. 1a). The initiation of the epoxide ring on the epichlorohydrin molecule was facilitated by the branched-PEI 1.2 kDa, leading to the formation of str-ZnO@PEI ($SN_2$ reaction; Supplementary Fig. 1b). Fine-tuning the molar ratio of str-ZnO to PEI yielded the optimal conditions (10:1), endowed with positive charges conducive to miRNA loading (Fig. 2b). Furthermore, Fourier-transform infrared (FTIR) spectroscopy revealed characteristic absorption bands of the amine group at 1628 $cm^{-1}$ (Supplementary Fig. 1c). To access the loading capacity of str-ZnO@PEI for miR-17 payload, gel electrophoresis and zeta potential measurements were performed (Fig. 2c and Supplementary Fig. 1d). Increasing the mass ratio of str-ZnO@PEI to miR-17 to 5:1 ensured the complete encapsulation of miR-17. Notably, the absence of miR-17 bands on the str-ZnO@PEI/miR-17 gel, in comparison with PEI/miR-17(5:1) alone, underscored the potential of str-ZnO as an effective carrier for PEI/miR-17. The 4 °C stability test showed that the complexes with the mass ratio of 5:1 remained stable for up to 7 days (Supplementary Fig. 1e).

Upon introducing str-ZnO into the GelMA hydrogels, notable changes in appearance were observed before and after cross-linking (Fig. 2d). The GelMA hydrogels gradually became whiter and less transparent, indicating the incorporation of str-ZnO. The SEM images of the cross-linked hydrogel (Fig. 2e) revealed a porous structure with str-ZnO uniformly dispersed on the surface, without causing any visible disruption to the original network-like porous microstructure. The successful embedding of str-ZnO within the GelMA hydrogels was further confirmed by elemental mapping of Zn (Supplementary Fig. 1f). In addition, the intensity of the str-ZnO diffraction peaks in the composite hydrogel increased with str-ZnO content (Supplementary Fig. 1g). Characteristic absorption bands at 644 and 548 $cm^{-1}$, corresponding to the stretching vibrations of the Zn-O bond, were also observed in the FTIR analysis (Fig. 2f). These findings collectively demonstrated the successful encapsulation of ZnO within the GelMA hydrogels matrix.

Subsequently, the MMP-triggered drug release from the str-ZPM Gel was evaluated in vitro. Figure 2g shows that the presence of collagenase II solution (simulating MMP overexpression in an OA environment) triggered the release of str-ZnO@PEI/miR-17 complexes from the str-ZPM Gel, resulting in a cumulative release of up to 66% over 7 days. This phenomenon can be attributed to the varying rates of hydrogel degradation under distinct conditions. The release profile of miR-17 from the str-ZnO@PEI/miR-17 complexes at pH 5, which simulates the intracellular lysosomal environment, showed a cumulative release of up to 71% miR-17 over 48 h (Supplementary Fig. 1h). In vitro hydrogel degradation experiments demonstrated that the incorporation of str-ZnO into the GelMA hydrogels impeded their degradation, ensuring sustained drug release for therapeutic efficacy. This effect was attributed to the interaction between the str-ZnO and the hydrogel, which led to the breaking of more chemical bonds by the degrading enzyme (Fig. 2h). Notably, hydrogel degradation was more pronounced after 21 days when immersed in an aqueous solution of collagenase II than immersion in PBS (Fig. 2i). The in vivo retention of the str-ZPM Gel was monitored using fluorescence imaging at the indicated time points (Supplementary Fig. 2a). The fluorescence signal decayed to 12% by day 28, indicating a gradual decrease in str-ZPM Gel accumulation at the tissue level (Supplementary Fig. 2b). By day 36, no positive signal was observed, suggesting that almost no residual str-ZPM Gel was detected at the tissue level.

### High-curvature str-ZnO modulates hydrogel rheological behavior

Oscillatory rheology was used to evaluate the mechanical properties of the hydrogels. The results showed an increase in the storage modulus (G′) of the composite hydrogel with an elevated concentration of str-ZnO. This increase can be attributed to the ability of str-ZnO to form cross-linked bonds with collagen as well as its inherent rigidity (Supplementary Fig. 3a). However, when the hydrogel was doped with 2% str-ZnO, the modulus decreased to 4 kPa. This decrease can be

https://doi.org/10.1038/s41467-025-59725-y

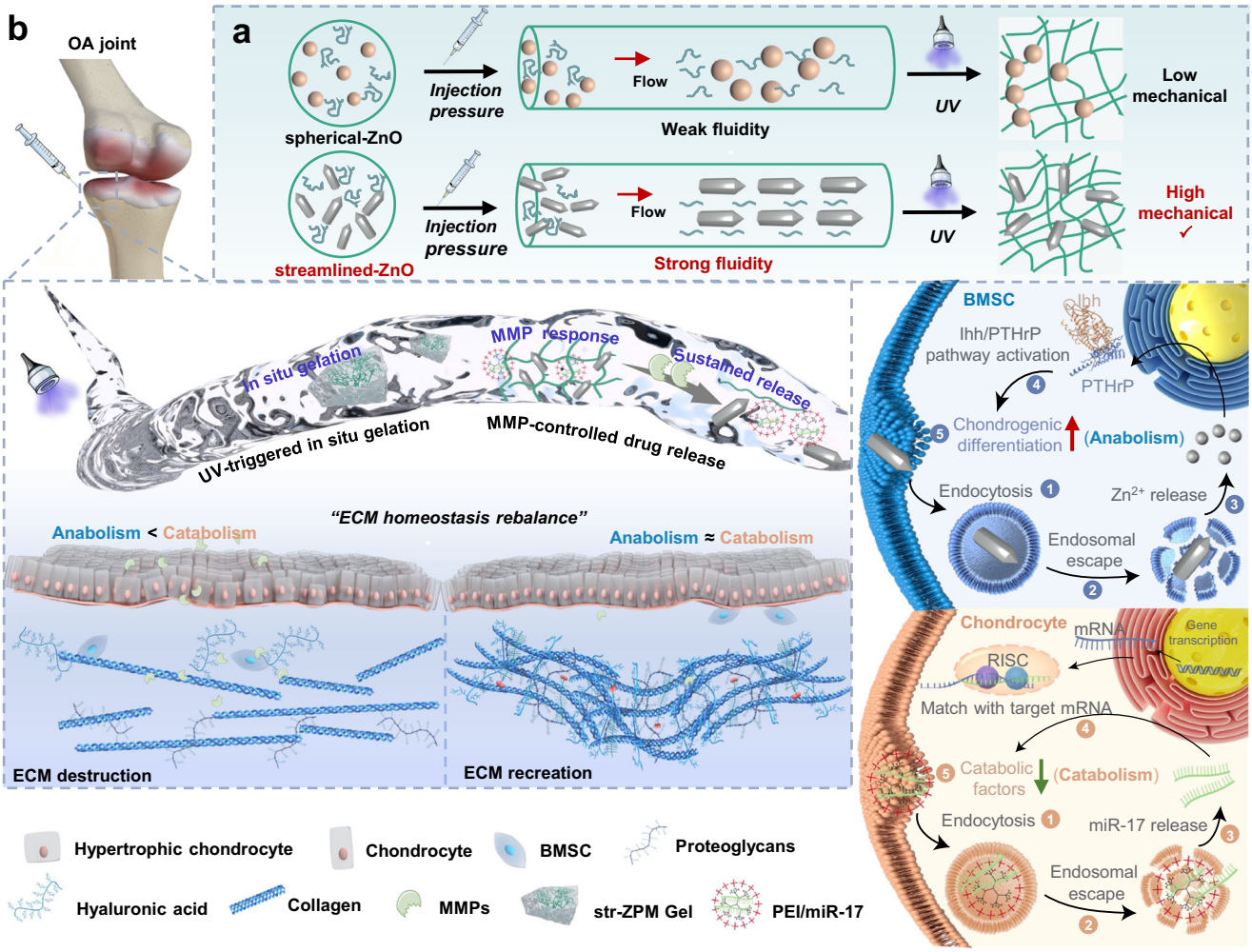


**Fig. 1 | ECM homeostasis rebalanced by miRNA-laden streamlined metal for controlling mechanical hydrogel facilitates stem cell differentiation. a** Diagram of the effect of different morphologies of ZnO on the hydrogel. **b** The mechanism of the str-ZPM Gel for cartilage ECM homeostasis modulation.

attributed to the apparent agglomeration of ZnO at high concentrations, which results in stress concentrations and a subsequent decline in the mechanical properties of the composite hydrogels[30–33]. Meanwhile, the G′ of all the cross-linked hydrogels exceeded G″, indicating the dominance of elastic behavior in the hydrogels (Supplementary Fig. 3b). Even when subjected to a large strain of 200% multiple times, which disrupts the gel structure in the nonlinear region, the rheological viscoelastic behavior of the sample remained unchanged when a small strain of 1% (i.e., in the linear region) was applied again. This observation suggests that the gel exhibited a strong capacity to resist strain recovery (Supplementary Fig. 3c).

Inspired by the notable impact of nanoparticle shape on drug delivery and cellular uptake rate[34–36], our study aimed to investigate the potential of nanoparticle morphology in modulating the rheological behavior and mechanical properties of hydrogel materials. A range of nanoparticles (NPs) has been successfully incorporated into natural polymeric networks, known as nanocomposite hydrogels, for applications in biological environments. Among them, spherical NPs have received the most attention[37]. Considering this, we synthesized hydrogels doped with spherical ZnO (sph-ZnO) to serve as a baseline for comparison with hydrogels containing non-spherical str-ZnO. The X-ray diffraction (XRD) pattern (Supplementary Fig. 3d) exhibited diffraction peaks corresponding to the wurtzite crystal structure of the str-ZnO NPs. The sharp and intense diffraction peaks indicated high crystallinity.

The rheological properties of the initial sol play a crucial role in the final gel processing. Consequently, we initially conducted a study to examine the rheological behavior of the sol. As the shear rate increased, both samples exhibited shear-thinning behavior, as depicted in Fig. 3a. In particular, the viscosity of str-ZnO decreased more rapidly, indicating a pronounced shear-thinning effect. At equivalent shear rates, the 0.5% str-ZnO sample exhibited a lower viscosity than the 0.5% sph-ZnO sample, suggesting that str-ZnO dispersed more rapidly within the cartilage defect during injection, potentially enhancing defect area repair (Fig. 3b and Supplementary Fig. 3e). However, what endowed the str-ZnO-doped hydrogels with exceptional fluidity and dispersion during injection? Recent studies by Jiang et al.[38] identified that the high curvature of the carrier significantly reduced the fluid resistance caused by pressure gradients, thereby accelerating the migration velocity of the carrier during the vascular extravasation process. These results suggest that non-spherical str-ZnO may positively enhance hydrogel fluidity. A representative transmission electron microscopy (TEM) image (Fig. 3c) illustrated the distinctive streamlined morphology of the str-ZnO NPs with average widths and lengths of approximately 30 nm and 150 nm, respectively. In addition, the curvature of each point and its variation along the surface of the NPs were depicted, with the apical endpoint exhibiting a greater mean curvature for str-ZnO than that for sph-ZnO (Fig. 3d). In alignment with the findings of Jiang et al., we hypothesized that NPs with high curvature and streamlined geometries, composed of ZnO, would also exhibit low fluidic resistance when embedded in hydrogel

https://doi.org/10.1038/s41467-025-59725-y

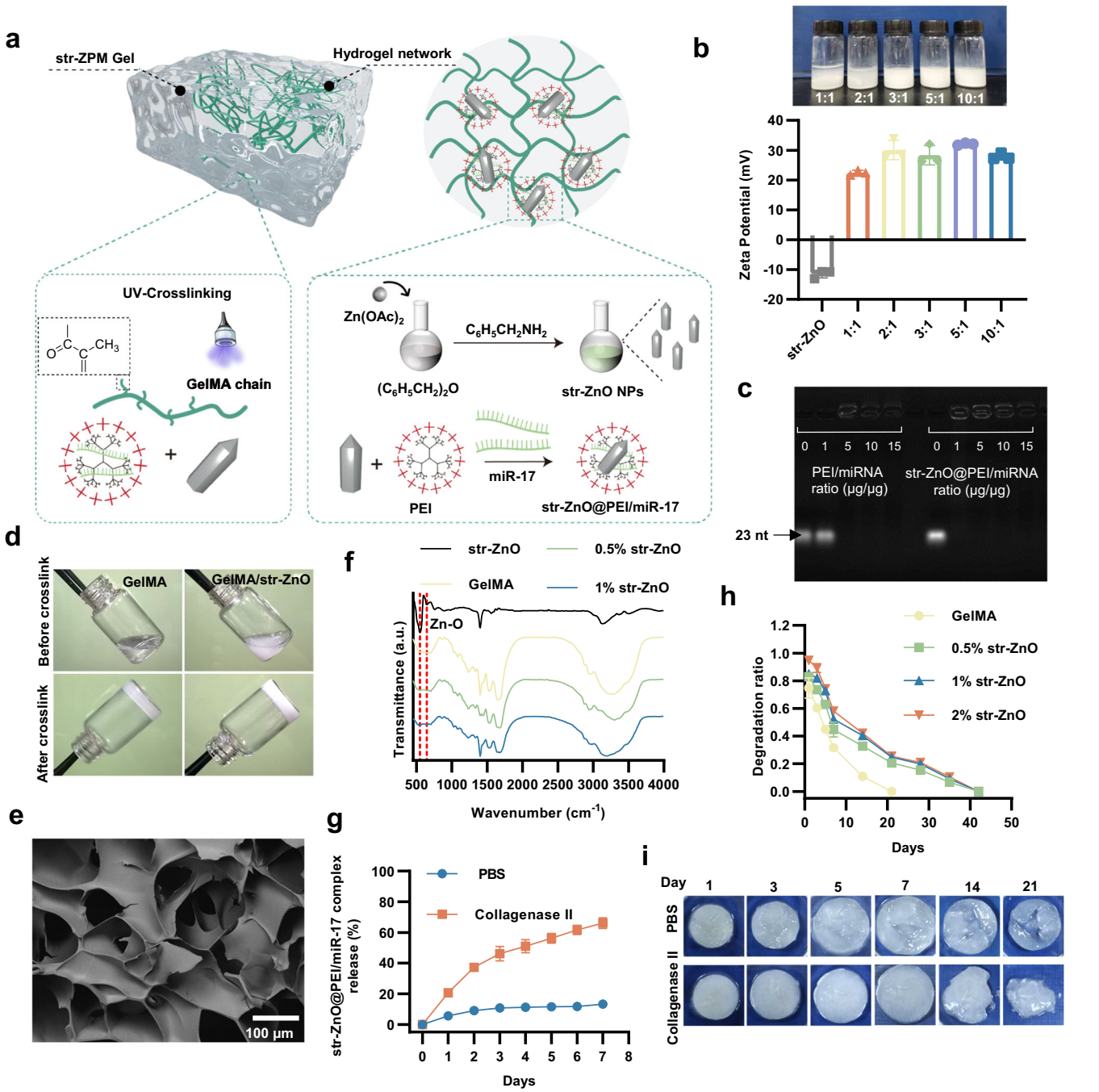


**Fig. 2 | Preparation and characterization of str-ZnO NPs and str-ZPM Gel.** **a** Synthesis of streamlined ZnO NPs and str-ZPM Gel. **b** Zeta potential of str-ZnO with PEI at different molar ratios. Data are presented as the mean ± SD ($n = 3$ independent experiments). **c** Agarose gel electrophoresis assays for PEI/miR-17 and str-ZnO@PEI/miR-17 at various mass ratios. The experiments were repeated three times independently. **d** The gelling process of GelMA and GelMA/str-ZnO (1%). **e** SEM image of str-ZPM Gel ($n = 3$ independent experiments). **f** FTIR spectra of str-ZnO, GelMA, GelMA/str-ZnO (0.5%), and GelMA/str-ZnO (1%). **g** The in vitro MMP-dependent release profile of the str-ZnO@PEI/miR-17 complex from str-ZPM Gel over 7 days. Data are presented as the mean ± SD ($n = 3$ independent experiments). **h** Degradation ratio of different hydrogels in collagenase II (100 μg/mL) aqueous solution. Data are presented as the mean ± SD ($n = 3$ independent experiments). **i** Images of hydrogels degradation when incubated in PBS and collagenase II (100 μg/mL) aqueous solution. Source data are provided as a Source Data file.

matrices. This reduction in fluidic resistance helps minimize energy loss, thereby boosting the diffusion rate of the particles. To test this hypothesis, nanoparticle tracking analysis (NTA) was employed to characterize the trajectories and quantitatively assess the diffusion coefficients of ZnO NPs with varying curvatures in the sol. Figure 3e, f illustrates the comparative behavior of str-ZnO and sph-ZnO in response to the injection forces. Str-ZnO possessed a superior ability to maintain a linear trajectory and shows enhanced directionality. Conversely, sph-ZnO displayed a notable tendency to deviate from this linear path to a certain degree. Under identical applied forces, str-ZnO achieved a longer gliding distance and superior motion efficiency. Figure 3g shows that str-ZnO with high curvature has an elevated effective diffusion coefficient, reaching a value of 3.2 $\mu m^2/s$. The results showed that high-curvature str-ZnO had an elevated effective diffusion coefficient, indicating reduced resistance during fluid movement and supporting our initial hypothesis. In conclusion, strategic local doping

https://doi.org/10.1038/s41467-025-59725-y

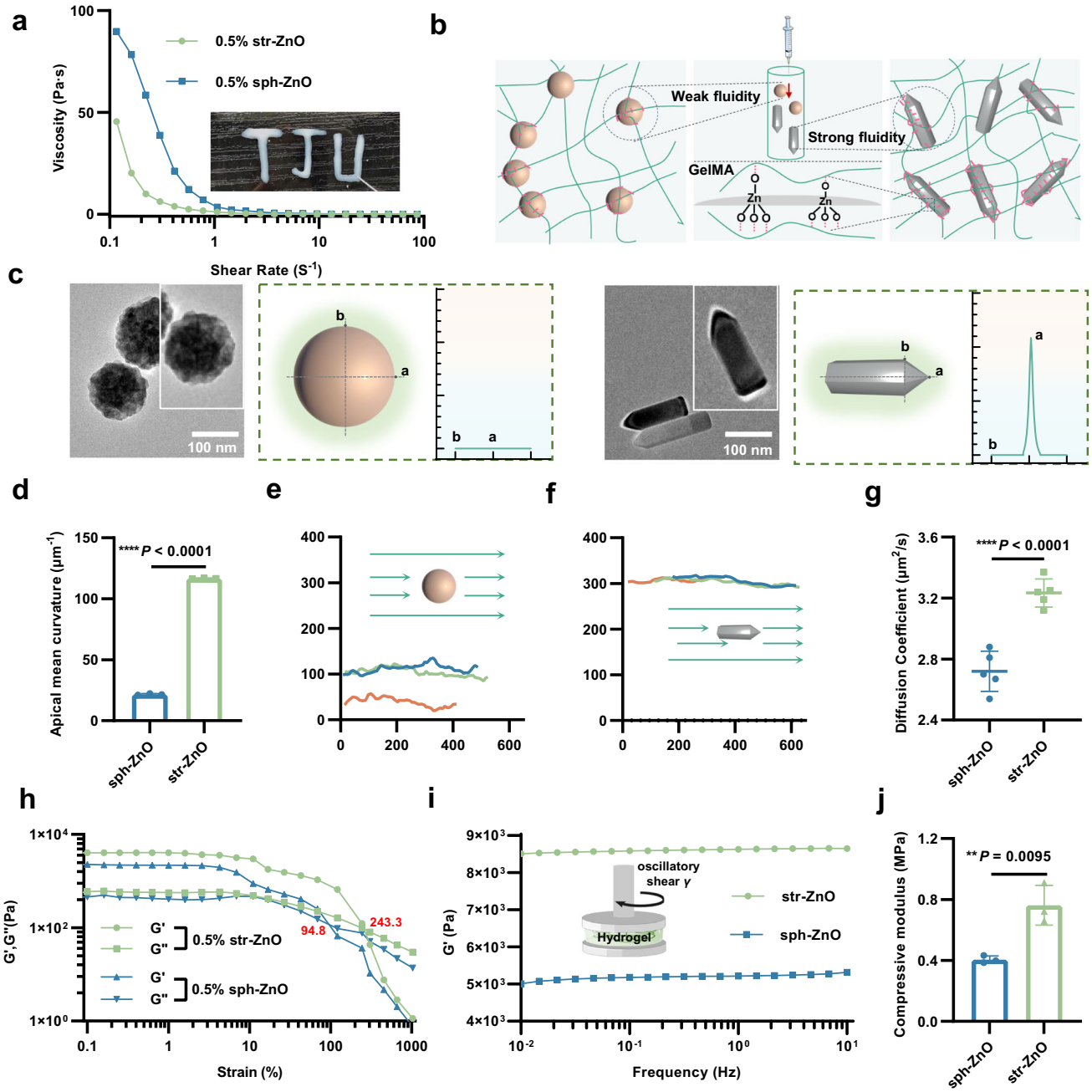


**Fig. 3 | Rheological behavior and mechanical properties of hydrogel using ZnO NPs of different morphologies. a** Comparison of the viscosity of different morphologies of ZnO with the shear rate from 0.1 to 100 $s^{-1}$. Inset: Photographs of the injectability of GelMA/str-ZnO hydrogel through the needle. **b** Schematic of the effect of different morphology of ZnO on the rheological behavior and mechanical properties of hydrogels. **c** Left: TEM images; Middle: Scheme of NPs; Right: Curvature distribution. a for the apical endpoint, b for the blunt endpoint. **d** Apical mean curvatures of sph-ZnO and str-ZnO. Data were presented as the mean ± SD ($n = 3$ independent experiments). **e** Trajectories of sph-ZnO in hydrogel at a syringe pump pressure of 100 μL/min. **f** Trajectories of str-ZnO in hydrogel at a syringe pump pressure of 100 μL/min. **g** The diffusion coefficient of sph-ZnO and str-ZnO in hydrogel. Data were presented as the mean ± SD ($n = 5$ independent samples). **h** Comparison of strain at the flow point between different morphologies of ZnO. **i** Comparison of storage modulus between different morphologies of ZnO. Inset: Schematic of oscillatory rheological testing. **j** Comparison of compressive modulus between different morphologies of ZnO. Data are presented as the mean ± SD ($n = 3$ independent experiments). $^{*}P < 0.05$, $^{**}P < 0.01$, $^{***}P < 0.001$, and $^{****}P < 0.0001$. Statistical comparisons were performed using the unpaired two-sided Student's *t*-test in **d**, **g**, **j**. Source data are provided as a Source Data file.

with str-ZnO significantly enhanced the fluidity of the sol, leveraging its fluid dynamics advantages, which is a valuable asset for injectable hydrogel applications.

In tissue engineering and drug delivery, a comprehensive evaluation of the rheological and mechanical properties of hydrogels is essential to ensure material suitability during critical application stages, such as injection, filling, tissue integration, and structural support provision. Through oscillatory rheology analysis, we observed an enhanced strain at the flow point (the crossover point of G′ and G″) for str-ZnO hydrogels, allowing them to endure shear strains of ~243.3% at the point of failure, compared to ~94.8% for sph-ZnO hydrogels (Fig. 3h). This finding indicates that str-ZnO hydrogels exhibit greater resistance to shear-induced instability, withstanding 2.6 times higher shear strains than their spherical counterparts.

Furthermore, the incorporation of 0.5% str-ZnO into GelMA hydrogels resulted in a 1.6-fold increase in the G′ compared to that of 0.5% sph-ZnO hydrogels (Fig. 3i). This significant enhancement in G′ could have a profound impact on the overall macroscopic mechanical strength of the composite hydrogel. Additionally, the compression experiments demonstrated that the hydrogels containing 0.5% str-ZnO exhibited superior compressive modulus (≈0.76 MPa) compared to those containing 0.5% sph-ZnO (≈0.41 MPa) (Fig. 3j). Furthermore, the cross-point strain exhibited a significant change with varying concentrations of str-ZnO, which was not observed for sph-ZnO (Supplementary Fig. 3f, g). This behavior can be ascribed to the stronger interaction between str-ZnO and the hydrogel network, resulting in an enhanced mechanical resistance to shear forces. These findings further support the crucial role of the nanoparticle morphology in determining the mechanical properties of hydrogels. Hydrogel reinforcement is commonly understood to occur through the interaction of nanoparticles, which serve as reversible crosslinkers spanning multiple polymer chains. This mechanism efficiently disperses stress across the network and dissipates it by disrupting nanoparticle–polymer crosslinks[39]. For example, cellulose nanofibers, with their significant specific surface areas, can form sacrificial hydrogen bonds that aid in stress dissipate[40]. By increasing the aspect ratio of str-ZnO to approximately 4.0, a marked expansion in the surface area was achieved during the formation of ZnO (Supplementary Fig. 3h). The enhanced mechanical properties of the str-ZnO-embedded hydrogels were attributed to the high specific surface area of str-ZnO, which enabled the formation of more sacrificial hydrogen bonds with neighboring polymer chains. These bonds can absorb and dissipate applied stress upon breakage (Supplementary Fig. 3i).

### Str-ZPM Gel facilitates gene transfection in vitro and extends the effect in vivo

The biocompatibility and potential cytotoxic effects of implanted biomaterials are crucial factors that require meticulous assessments to ensure the safety and efficacy of their clinical applications. In this study, various hydrogels were co-cultured with chondrocytes and BMSCs for 1, 3, and 5 days using a Transwell system (Fig. 4a). Live/dead staining results demonstrated a predominance of viable cells in both groups, indicating that the hydrogels were not significantly cytotoxic (Supplementary Fig. 4a–d). Quantitative analysis of cell viability using the CCK-8 assay revealed an increased proliferative activity in chondrocytes and BMSCs treated with 0.5% str-ZnO, whereas 1% str-ZnO showed no significant effect (Supplementary Fig. 4e, f). Furthermore, CCK-8 demonstrated favorable cytocompatibility for both the sph-ZPM Gel and str-ZPM Gel (Fig. 4b). Subsequently, we accessed the cell adhesion and growth morphology on the hydrogels with different concentrations of str-ZnO. After 2 days of culture, the cytoskeleton was stained with Phalloidin-TRITC. The results demonstrated that both chondrocytes and BMSCs exhibited good adhesion and spreading on the surface of the 0.5% str-ZnO hydrogels, with clear actin filament stretching, indicating a minimal impact of the hydrogel on cell morphology. However, an increased contraction of cell morphology was observed when the concentration of str-ZnO was increased to 1% (Supplementary Fig. 5a). In addition, quantitative analysis of the images revealed a larger cell spreading area on the surface of 0.5% str-ZnO for both cell types. In particular, the diffusion area of BMSCs on the hydrogel was 1.2 times larger than that of the control group, illustrating the stronger affinity of BMSCs for the 0.5% str-ZnO hydrogel (Supplementary Fig. 5b, c). In conclusion, a composite hydrogel with a low concentration of str-ZnO (0.5%) exhibited excellent biocompatibility and could be used for further experimental investigations. To evaluate the uptake of str-ZnO@PEI/miR-17 by BMSC and chondrocytes, FITC-labeled str-ZnO was used for cell culture. A distinct green fluorescent signal was observed upon co-localization with confocal laser scanning microscopy (CLSM), indicating that the str-ZnO@PEI/miR-17 complex was internalized by cells via the endocytic pathway (Supplementary Fig. 5d). Immunofluorescence observations revealed that the str-ZPM Gel facilitated the expression of SOX9, indicating the differentiation of BMSCs into chondrocytes (Fig. 4c, Supplementary Fig. 5e). These results demonstrated that the str-ZPM Gel could provide an ECM-mimicking structure and release str-ZnO@PEI/miR-17, which can be taken up by cells without cytotoxicity.

Based on previous studies on the effect of nanoparticle shape on cellular phagocytosis, a comparison was made between sph-ZnO- and str-ZnO- transfected miR-17 (Fig. 4d). The transfection efficiency of sph-ZnO and str-ZnO on chondrocytes was first evaluated by comparing the fluorescence intensity using CLSM at 24 h (Fig. 4e). The expression level of miR-17 in str-ZnO-treated cells exhibited a significant increase (~3.5 folds higher than that in sph-ZnO-treated cells), which was further confirmed by qRT-PCR (Table S1 and Fig. 4f, g). To gain a deeper insight into the mechanism underlying the increased transfection efficiency of str-ZnO, we assessed the cellular uptake and endosomal escape efficiency of different forms of ZnO (Fig. 4h and Supplementary Fig. 5f, g). Our findings indicated that str-ZnO exhibits enhanced internalization and more efficient escape from endosomes within the same timeframe (Supplementary Fig. 5h, i), potentially contributing to its superior transfection efficiency. We hypothesized that the streamlined morphology of str-ZnO enables easier penetration through the cell membrane, thereby promoting the enhanced endocytosis of gene vectors. To investigate the in vivo effects of released miR-17 on OA, we surgically implanted both sph-ZPM Gel and str-ZPM Gel into rat knee joints. After 4 weeks, fluorescence in situ hybridization (FISH) analysis of the harvested joints revealed a higher miR-17 expression level in the str-ZPM Gel group than that in the sph-ZPM Gel group, suggesting that the release of miR-17 from the str-ZPM Gel might have a prolonged effect on attenuating OA (Fig. 4i and Supplementary Fig. 5j). When rat chondrocytes were exposed to the proinflammatory factor IL-1β in culture, a notable upregulation of catabolic factors (MMP13 and ADAMTS5) was observed, a response partially mitigated by transfection of miR-17 (Fig. 4j). Notably, the str-ZPM Gel demonstrated higher efficiency in transferring miR-17 into chondrocytes than the sph-ZPM Gel, resulting in reduced catabolic factor production (Fig. 4k). Collectively, these findings indicated that str-ZnO can serve as an efficient vector for enhanced gene transfection.

To investigate the ability of the zinc ions released from the str-ZPM Gel to recruit BMSCs in vitro, a Transwell system was employed (Supplementary Fig. 5k). Staining and cell counting analysis performed on the trans-pore membrane indicated a substantial increase in the number of migrating cells in the str-ZPM Gel group compared to that in the control and GelMA groups, which was attributed to enhanced cell motility[41] (Supplementary Fig. 5l, m). These findings confirm that the release of $Zn^{2+}$ during str-ZPM Gel degradation acts as a positive factor for BMSCs homing[42].

### str-ZPM Gel maintains ECM homeostasis by promoting BMSCs chondrogenic differentiation and suppressing catabolism

The chondrogenic differentiation-inducing capability of the str-ZPM Gel on BMSCs was evaluated in vitro using qRT-PCR after 7 and 21 days of culture in cartilage conditioned medium. The results revealed a significant increase in the mRNA levels of chondrogenic differentiation-related genes, such as SOX9, COL2A1, and Aggrecan, during the differentiation of BMSCs into chondrocytes. The mRNA expression of MMPl3 and ADAMTS5, which are associated with ECM degradation, was inhibited by the str-ZPM Gel (Fig. 5a). To mimic the chronic inflammatory environment in vivo, normal cells were treated with IL-1β (10 ng/mL). This stimulation resulted in a notable increase in the protein levels of MMP13 and ADAMTS5 in IL-1β-treated BMSCs

https://doi.org/10.1038/s41467-025-59725-y

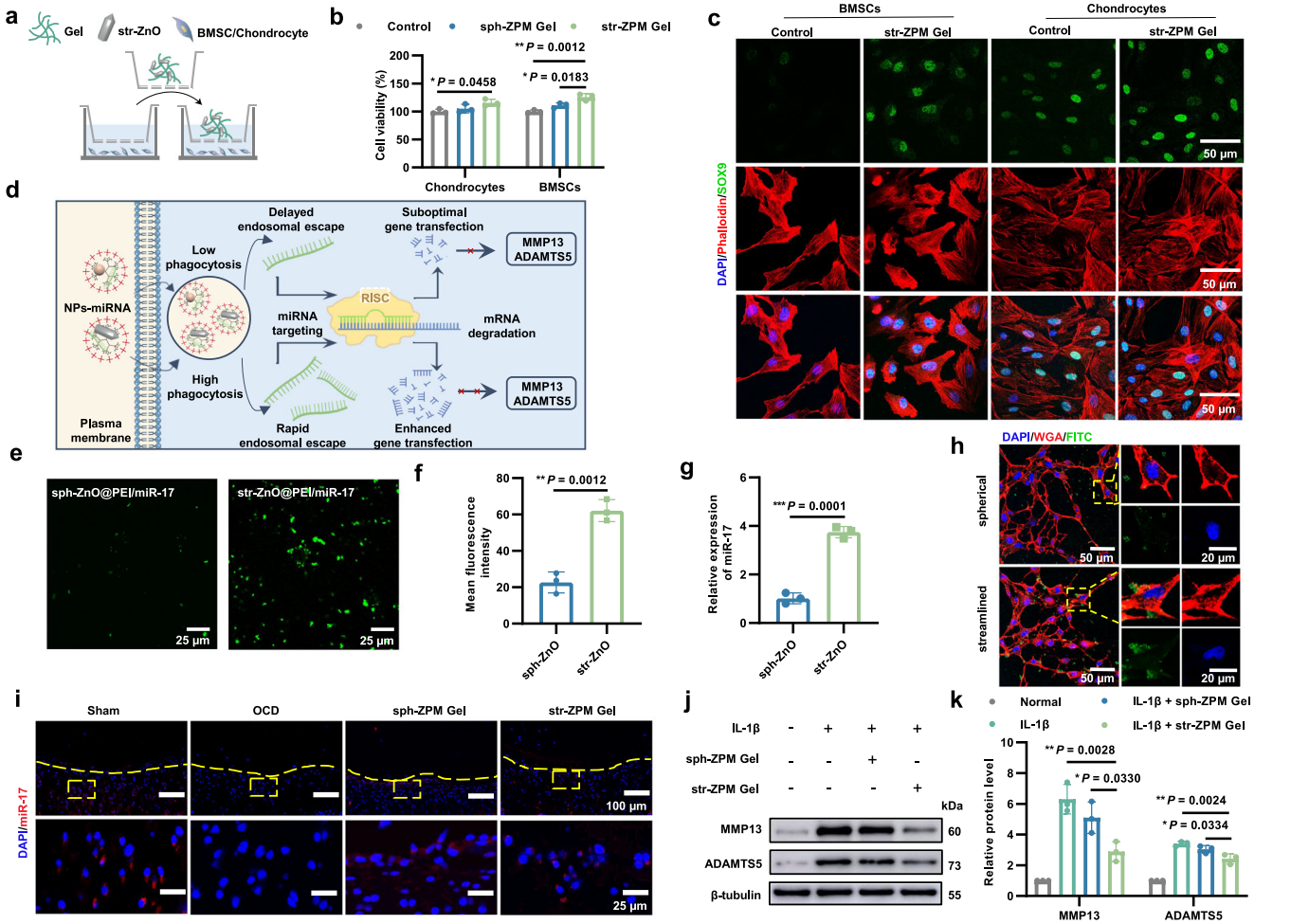


**Fig. 4 | Str-ZPM Gel facilitates gene transfection in vitro and extended effect in vivo. a** Schematic of chondrocytes or BMSCs in noncontact coculture with hydrogels in a 12-well transwell plate. **b** CCK-8 assay at 5 days. **c** Immunofluorescence staining of SOX9 of rat BMSCs and chondrocytes cultured with str-ZPM Gel for 5 days ($n = 3$ independent experiments). **d** Schematic comparison of the transfection process of sph-ZnO and str-ZnO. **e** Assessment of the in vitro gene transfection efficacy of sph-ZnO and str-ZnO on chondrocytes. **f** Quantitative analysis of mean fluorescence intensity. **g** Quantitative analysis of miR-17 expression at 24 h. **h** BMSCs were incubated with FITC-labeled streamlined and spherical ZnO for 15 min, and cellular uptake was analyzed ($n = 3$ independent experiments). Cell nuclei and cellular membranes were stained with DAPI (blue) and wheat germ agglutinin (red), respectively. **i** FISH analysis of miR-17 in rat knee cartilage at 4 weeks after surgery ($n = 3$ independent experiments). **j** Rat articular chondrocytes were incubated with sph-ZPM Gel or str-ZPM Gel and treated with or without IL-1β (10 ng/mL) for 24 h. The protein levels of catabolic factors were determined by Western blot. Blots are representative of three independent experiments. **k** Related quantitative analysis of protein expression levels. Data were presented as the mean ± SD ($n = 3$ independent experiments). $^{*}P < 0.05$, $^{**}P < 0.01$, and $^{***}P < 0.001$. Statistical comparisons were performed using the unpaired two-sided Student's *t*-test in **f**, **g** and one-way ANOVA with Tukey's test in (**b**, **k**). Source data are provided as a Source Data file.

(Fig. 5b, c). Upon treatment with str-ZPM Gel, alterations in MMP13 and ADAMTS5 were reversed. However, the effect of the str-ZP Gel (GelMA/str-ZnO@PEI/miR-NC) on the expression of MMP13 and ADAMTS5 was not significant. To confirm the pivotal role of miR-17 in maintaining ECM homeostasis, we introduced an miR-17 inhibitor concurrently. No substantial changes in MMP13 and ADAMTS5 protein expression were observed following treatment with the miR-17 inhibitor, indicating that miR-17 plays a role in mitigating ECM catabolism. Additionally, western blot analysis demonstrated that the intensity of SOX9, COL2A1, and Aggrecan protein bands (markers of anabolism) was significantly higher in both the str-ZP Gel and str-ZPM Gel groups. This suggests that str-ZnO possesses the ability to promote the differentiation of BMSC into chondrogenic cells. However, the precise role of $Zn^{2+}$ in cell differentiation remains unclear. Cell uptake experiments showed that str-ZnO was effectively internalized by BMSC in vitro, providing a basis for the promotion of chondrogenic differentiation through intracellular $Zn^{2+}$. Previous studies have highlighted the importance of the Ihh/PTHrP signaling pathway as a crucial regulator of chondrocyte differentiation and maturation[43,44]. Ihh and PTHrP regulate each other and play collaborative roles in controlling the differentiation and proliferation of human chondrocytes in vivo. Cyclopamine acts as a specific inhibitor of the Hh signaling pathway (Fig. 5d). Binding to the membrane receptor Smo within the signaling cascade effectively impedes the downstream signal response[45]. In this study, we used this inhibitory compound to block Hh signaling and evaluated its effect on the chondrogenic differentiation of BMSCs. Comparative analysis revealed a significant increase in the gray values of the Ihh and PTHrP protein bands within the str-ZPM Gel group compared to those in the control group (Fig. 5e, f). The expression of PTHrP, a recognized target gene of Ihh signaling[46], is downregulated upon cyclopamine treatment. In cultured rat BMSCs exposed to cyclopamine (5 μM) for 24 h, the expression of chondrogenic differentiation-related proteins (SOX9, Aggrecan, and COL2A1) was suppressed despite the increased concentration of $Zn^{2+}$ (Fig. 5g, h). These results strongly suggest that the Ihh/PTHrP pathway likely plays a pivotal role in regulating chondrogenic differentiation, which is potentially mediated by str-ZPM Gel.

https://doi.org/10.1038/s41467-025-59725-y

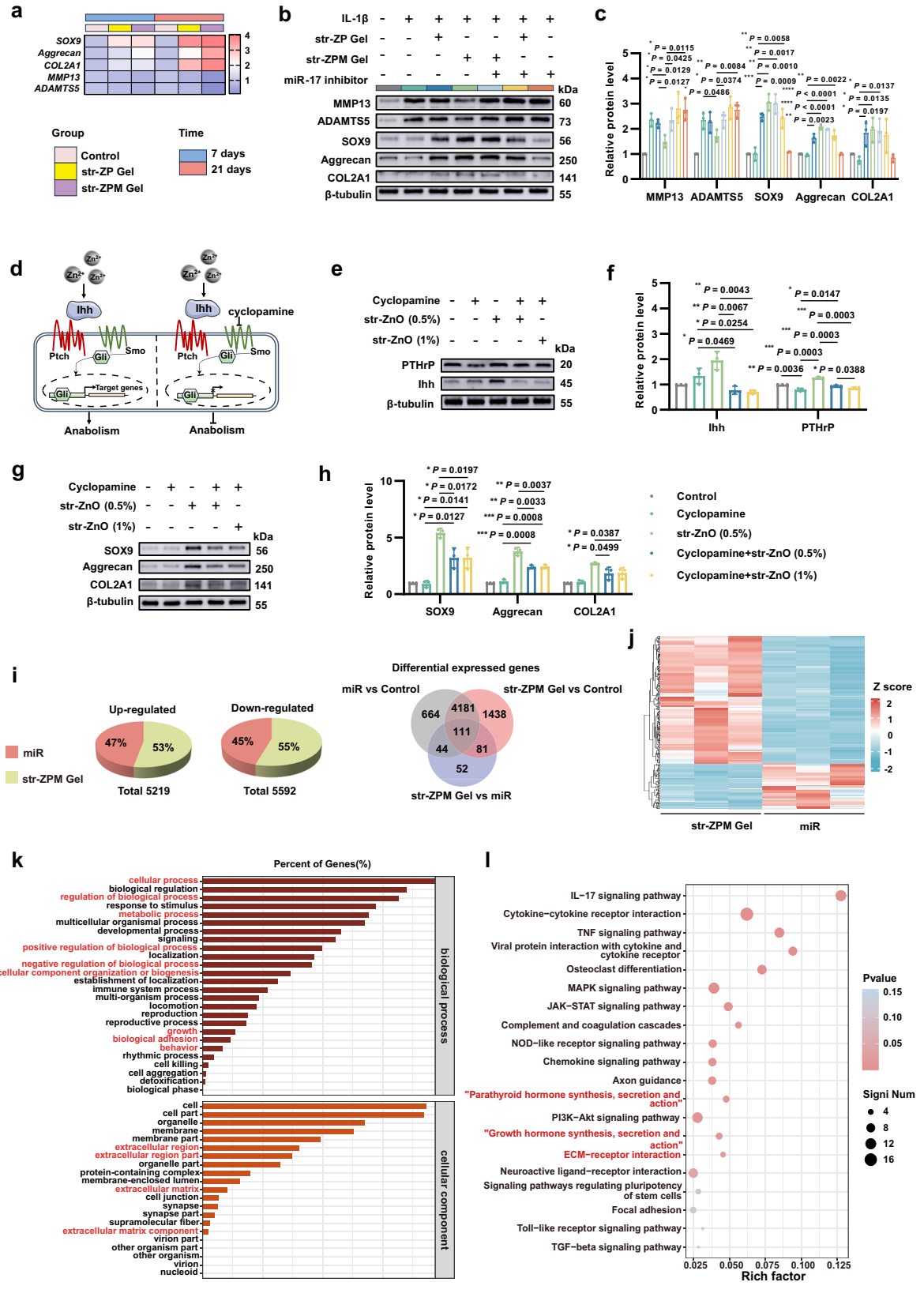


To gain deeper insight into the impact of the str-ZPM Gel on BMSCs recruitment and differentiation, mRNA sequencing analysis was conducted on BMSCs from the different groups after 7 days. Str-ZPM Gel treatment resulted in a considerable number of differentially expressed genes (DEGs) compared to the control group (Supplementary Fig. 6a). To elucidate the individual contributions of the components within the str-ZPM Gel, the effects of miR-17-5p (miR) and $Zn^{2+}$ on cell behavior were evaluated separately (Fig. 5j). A total of 10,811 differentially DEGs were identified in both the miR and str-ZPM Gel groups, with 5219 upregulated and 5592 downregulated genes. In addition, the Venn diagram showed that 1438 DEGs specific to the str-ZPM Gel group, and 664 DEGs were specific to the miR group

**Fig. 5 | str-ZPM Gel maintains ECM homeostasis by promoting BMSCs chondrogenic differentiation and suppressing catabolism. a** qRT-PCR analysis of gene expression of SOX9, COL2A1, Aggrecan, MMP13, and ADAMTS5 for 7 days and 21 days. **b** WB analysis of protein levels of MMP13, ADAMTS5, SOX9, Aggrecan, and COL2A1 in normal and IL-1β-treated BMSCs cultured with hydrogels for 7 days. **c** Related quantitative analysis of protein expression levels. **d** Diagram of the mechanism of chondrogenic differentiation of BMSCs. **e** WB analysis of protein levels of Ihh and PTHrP in normal and cyclopamine-treated BMSCs cultured with hydrogels for 7 days. **f** Related quantitative analysis of Ihh and PTHrP expression levels. **g** WB analysis of anabolic-related protein levels in normal and cyclopamine-treated BMSCs cultured with hydrogels for 7 days. **h** Quantitative analysis of the expression levels of anabolic-related proteins. **i** Differentially expressed mRNA in miR, and str-ZPM Gel groups ($Q$ values <0.05, $|\log_2(\text{fold change})|$ >2). **j** Heatmap showing the hierarchical clustering of the differentially expressed genes in miR and str-ZPM Gel groups. **k** GO enrichment bar plots of str-ZPM Gel and miR groups. **l** KEGG pathway enrichment analysis of the identified DEGs of the str-ZPM Gel groups vs the miR groups. Blots are representative of three independent experiments in **b**, **e**, and **g**. Data were presented as the mean ± SD ($n = 3$ independent experiments). $^{*}P < 0.05$, $^{**}P < 0.01$, and $^{***}P < 0.001$. Statistical comparisons were performed using the unpaired two-sided Student's $t$-test in **c**, **f**, and **h**. Source data are provided as a Source Data file.

compared to the control group (Fig. 5i). Gene ontology (GO) analysis across the three groups indicated a strong correlation of DEGs with the extracellular matrix component/region as well as cell adhesion, proliferation, and migration (Fig. 5k and Supplementary Fig. 6b). Additionally, Kyoto Encyclopedia of Genes and Genomes (KEGG) pathway analysis demonstrated the enrichment of functional annotations related to cell adhesion, ECM-receptor interactions, and signaling pathways regulating the pluripotency of stem cells, which are involved in cartilage repair (Supplementary Fig. 6c). Notably, the str-ZPM Gel group exhibited enrichment of parathyroid hormone synthesis, secretion, and action compared to the miR group, indicating effective stimulation of BMSCs by $Zn^{2+}$ (Fig. 5l).

## str-ZPM Gel induces BMSCs recruitment and rescues OA cartilage degeneration in rats

Building on the in vitro observations, we conducted further assessments to explore the effects of str-ZPM Gel on the recruitment of BMSCs in vivo. At 7- or 14-days post hydrogel implantation, the joints were stained with CD90 and CD44 (critical markers of BMSCs) (Fig. 6a). The results demonstrated that BMSCs in the str-ZPM Gel group were distributed in clusters or layers[47] around the defect area and exhibited infiltration into the cartilage surface by day 14, indicating their potential to differentiate into chondrocytes (Fig. 6b). Additionally, after 4 weeks, the average concentration of $Zn^{2+}$ in cartilage tissues from the sham-operated group averaged 2.2 μmol/gp rot, whereas in cartilage tissue implanted with str-ZPM Gel, this concentration notably increased to 2.9 μmol/gprot (Supplementary Fig. 7). This indicates that the zinc-based hydrogels effectively release zinc ions, potentially promoting cartilage repair and regeneration. By the 8-week mark, the concentration of $Zn^{2+}$ significantly decreased, indicating the potential absorption and metabolism of recently released metal ions by local tissues. An OA rat model was established using a cylindrical cartilage defect (Supplementary Fig. 8) to assess the in vivo therapeutic efficacy of the str-ZPM Gel based on the treatment protocol (Fig. 6c). To examine the impact of the str-ZPM Gel on ECM homeostasis regulation in rats, the expression of relevant proteins in cartilage tissues was measured after 2 weeks of treatment (Fig. 6d). Quantitative analysis revealed an increase in the expression of anabolism-related proteins (COL2A1 and Aggrecan) and a decrease in the expression of catabolism-related proteins (MMPl3 and ADAMTS5) (Fig. 6e). Furthermore, key proteins involved in the Ihh/PTHrP signaling pathway were also upregulated in the str-ZPM Gel treatment group, consistent with the in vitro findings, thus demonstrating the effective regulatory effect of str-ZPM Gel in vivo. The macroscopic morphology of the regenerated cartilage was observed at 4 and 8 weeks postoperatively to evaluate the efficacy of the str-ZPM Gel in cartilage regeneration (Fig. 6f). At 4 weeks, the OCD group exhibited a distinct cavity with a clear border of surrounding normal tissue. In the str-ZP Gel group, a small amount of new tissue was observed in the defect area, accompanied by surface roughness. Conversely, the defect area in the str-ZPM Gel group was covered with a relatively large amount of regenerated tissue, albeit with a slight surface crack. At 8 weeks, the OCD group exhibited the most severe cartilage defects among all the groups, whereas the new tissue surface in the gel group was completely smooth and well-integrated with the surrounding tissue. According to the International Cartilage Repair Score (ICRS) standard (Table S2)[48], the macroscopic scoring results clearly demonstrated that regeneration in the str-ZPM Gel group surpassed that in the other groups (Fig. 6g, h). Subsequently, we conducted micro−computed tomography (micro-CT) to assess the osteophyte volume within the knee joint (Fig. 6i). The reconstructed micro-CT images clearly illustrated a notable decrease in osteophyte formation within the str-ZP Gel and str-ZPM Gel groups (marked in red). Conversely, untreated rats with knee cartilage injury exhibited a significant increase in osteophyte formation post-surgery (Fig. 6j). Furthermore, compared with those in the OCD group, the bone microstructure parameters (BMD, BV/TV, Tb. N, and Tb. Th) improved with str-ZP Gel treatment, and these parameters were further enhanced in the str-ZPM Gel group (Fig. 6k–n). In addition, the str-ZPM Gel led to a reduction in Tb. Sp, which showed minimal changes after str-ZP Gel treatment (Fig. 6o). Based on the aforementioned findings, we conclude that the str-ZPM Gel has the potential to alleviate OA by reducing osteophytes in the subchondral bone.

## Evaluation of str-ZPM Gel regeneration efficacy in vivo

The BioScience atomic force microscope was utilized to perform a biomechanical analysis of the repaired cartilage area at 8 weeks post-surgery, as illustrated in Fig. 7a. The findings showcased a significantly increased elastic modulus value (0.40 ± 0.11 GPa) in the cartilage repaired with str-ZPM Gel when compared to both the OCD (0.08 ± 0.02 GPa) and str-ZP Gel groups (0.16 ± 0.03 GPa) (Fig. 7b). Furthermore, the surface repairs of the articular region in the OCD and str-ZP Gel groups exhibited roughness in contrast to the smoother surface observed in the sham-operated cartilage. Notably, the integration and smoothness of the cartilage surface regenerated with the str-ZPM Gel closely mirrored those of the sham-operated group. The CatWalk gait analysis system was used to detect subtle alterations in the rat motor performance. Intuitively, rats from the str-ZPM Gel group demonstrated a more coordinated gait, while those in the OCD group did not exhibit restoration of hind limb support (Supplementary Fig. 9). Additionally, the left hind limb injected with the hydrogel was analyzed independently. Analysis of the data revealed no statistically significant differences in gait indices, including stand, print area, and mean intensity, between the str-ZPM Gel and the sham-operated groups. To examine the microstructure following recovery, we performed H&E, toluidine blue, and Safranin O−Fast Green staining of the local tissue (Fig. 7c and Supplementary Fig. 10). By week 8, newly formed cartilage tissues were evident in the defects treated with the str-ZP Gel and str-ZPM Gel. Contrarily, the regenerated tissue in the OCD group consisted mainly of fibrous tissue without the typical layered structure of cartilage formation, suggesting an insufficient self-healing capacity to repair cartilage at the defect site. Histological scores demonstrated a significant improvement in the morphology of the neo-formed surface tissue, thickness of the neo-formed cartilage, and regularity of the joint surface in the str-ZPM Gel group (Table S3 and Fig. 7d). Moreover, the histological score increased at 8 weeks compared to that at 4 weeks in the str-ZP Gel and str-ZPM Gel group, indicating a persistently improved cartilage repair effect. Conversely, the scores remained relatively constant in the OCD group (Fig. 7e).

https://doi.org/10.1038/s41467-025-59725-y

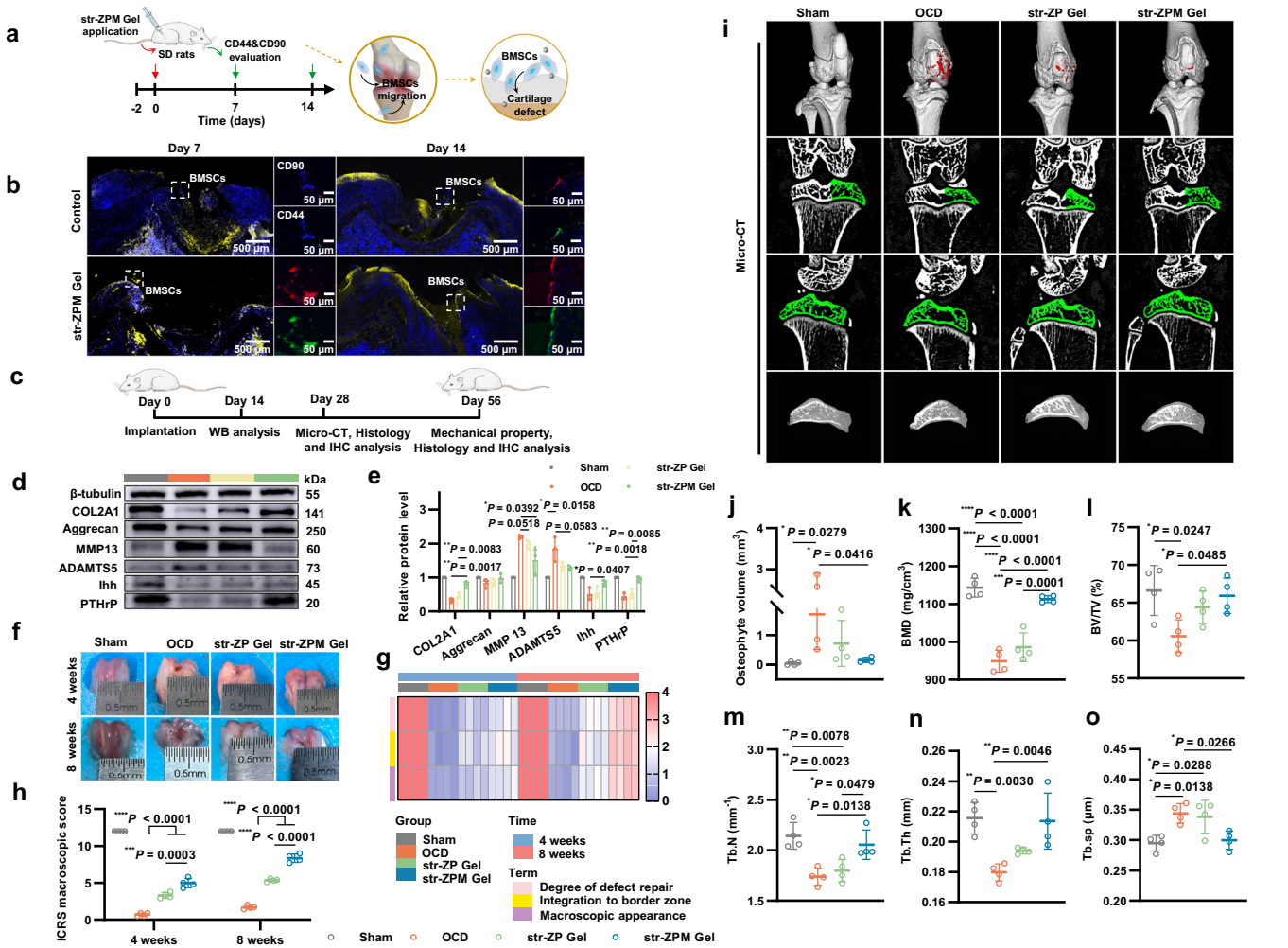


**Fig. 6 | str-ZPM Gel induces BMSCs recruitment and rescues OA cartilage degeneration in rats. a** Experimental design time flowchart and the illustration of the recruitment process of BMSCs during cartilage repair. **b** Immunofluorescent staining of CD44 and CD90 at 7 or 14 days. **c** Experimental design time flowchart. **d** WB analysis of protein levels of COL2A1, Aggrecan, MMP13, ADAMTS5, Ihh, and PTHrP in rats. Blots are representative of three independent experiments. **e** Quantitative analysis of WB. Data were presented as the mean ± SD ($n = 3$ independent experiments). $^{*}P < 0.05$, $^{**}P < 0.01$, and $^{***}P < 0.001$. Statistical comparisons were performed using the unpaired two-sided Student's *t*-test. **f** Macroscopic observation of cartilage defect at 4- and 8-weeks post-surgery. **g** Heatmap of variables of macroscopic scoring at 4 and 8 weeks. **h** ICRS macroscopic scores of different groups. Data were presented as the mean ± SD ($n = 4$ independent experiments). $^{*}P < 0.05$, $^{**}P < 0.01$, and $^{***}P < 0.001$. Statistical comparisons were performed using one-way ANOVA with Tukey's test. **i** Representative three-dimensional (3D) images of the rat knee joint, 2D images in the coronal and sagittal planes were reconstructed by micro-CT. (3D images of subchondral bone were obtained by reconstructing the green areas in 2D images using processing software). **j** Quantitative analysis of osteophyte volume. **k**–**o** BMD, BV/TV, Tb. N, Tb. Th, and Tb. Sp were quantified by micro-CT. Data were presented as the mean ± SD ($n = 4$ independent experiments). $^{*}P < 0.05$, $^{**}P < 0.01$, $^{***}P < 0.001$, and $^{****}P < 0.0001$. Statistical comparisons were performed using one-way ANOVA with Tukey's test in **j**–**o** Source data are provided as a Source Data file.

Subsequently, we investigated the chondrogenic differentiation and ECM homeostasis in the cartilage using immunohistochemical staining. In the str-ZPM Gel group, the stained region was strongly positive (dark brown) for Aggrecan, COL2A1, Ihh, and PTHrP, indicating that the str-ZPM Gel facilitated chondrogenic differentiation in vivo by regulating Ihh/PTHrP expression (Fig. 7f and Supplementary Fig. 11a–c). A contrasting trend (pale yellow) was observed for MMP13 expression. Quantitative assessment revealed an increase in Aggrecan and COL2A1-positive cells, along with a significant reduction in MMP13-positive cells within the str-ZPM Gel group at the 8-week mark (Fig. 7g–i). These changes were comparable to those observed in the sham group, indicating an increase in anabolism a and decrease in catabolism. Collectively, these results suggest that str-ZPM Gel exhibits a more favorable ability to repair OA by inducing BMSCs recruitment and promoting cartilage regeneration. We also harvested rats' hearts, livers, spleens, lungs, and kidneys 2 months after material implantation and performed H&E staining (Supplementary Fig. 12). The results showed no obvious organ damage or inflammation in the experimental groups, demonstrating their efficacy and long-term biosafety for clinical applications.

## Discussion

Current pharmacological approaches for treating OA primarily focus on providing symptomatic relief and short-term improvement in joint function[49]. However, in the early stages of OA, pathological changes occur in the cartilage ECM, leading to abnormal signaling in chondrocytes and triggering aberrant remodeling. This results in a vicious cycle that ultimately leads to disease[50]. Abnormal hypertrophic differentiation of chondrocytes and secretion of matrix-destroying enzymes, particularly MMP13 and ADAMTS5, directly degrade the ECM and disrupt catabolic process[51–53]. Additionally, aging gradually reduces the number of chondrocytes, resulting in a diminished matrix anabolic capacity[54,55]. Although most studies have focused on inflammatory responses and component changes, the correlation between

https://doi.org/10.1038/s41467-025-59725-y

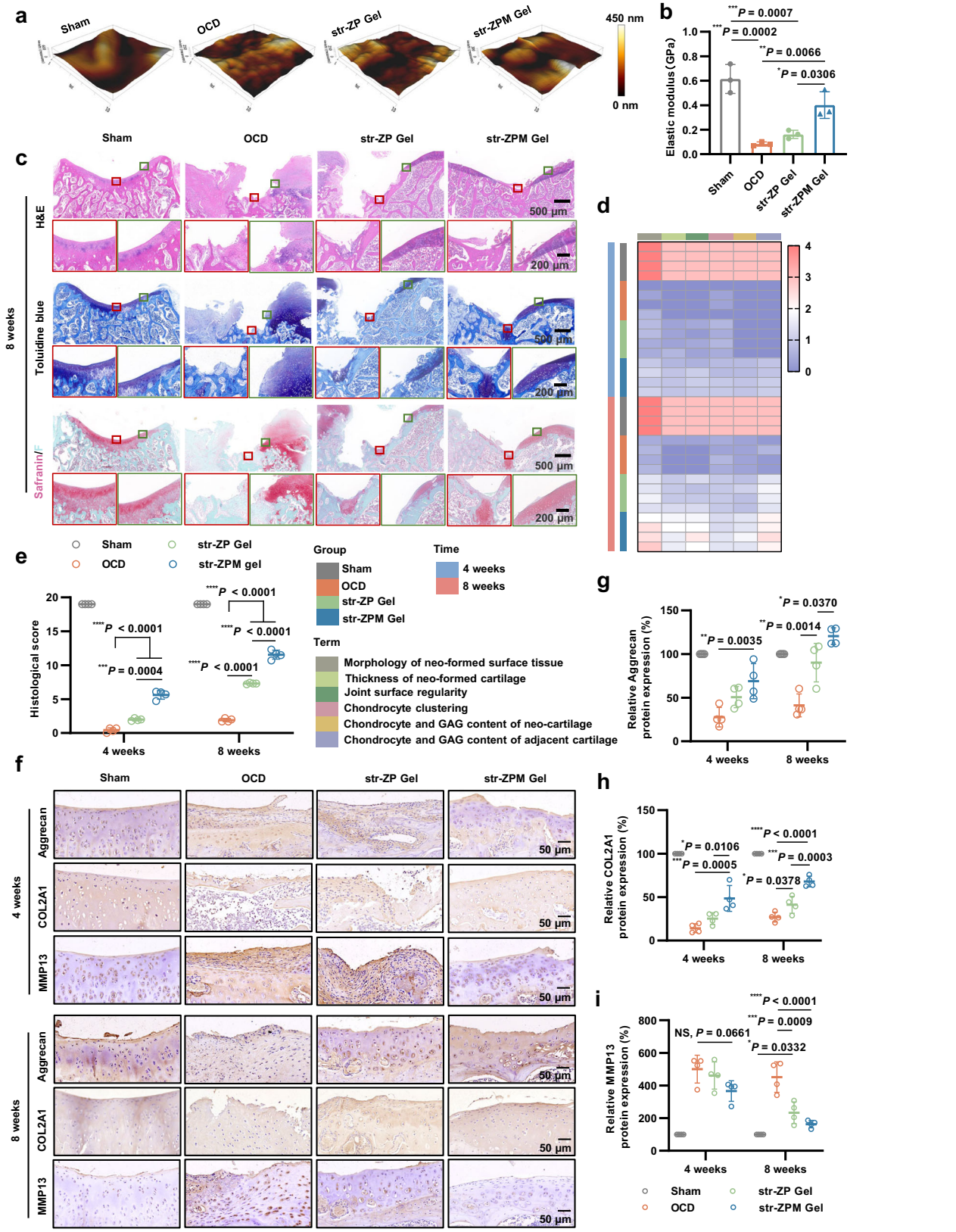


cartilage ECM changes and OA development has not been extensively explored[12,56,57]. In light of these observations, we aimed to address homeostatic abnormalities in the ECM and treat OA by rebalancing homeostasis through simultaneous enhancement of anabolism and suppression of catabolism. Due to the limited proliferative and regenerative capacities of senescent chondrocytes in OA, improving anabolism is challenging. Therefore, the BMSCs differentiation strategy is an excellent alternative cell source for generating new chondrocytes and promoting cartilage regeneration[58]. In this context, Ha et al. developed a GFOGER-modified hydrogel incorporating exogenous BMSCs, which significantly enhanced osteochondral defect regeneration in rats by activating integrin-mediated adhesion and

**Fig. 7 | Evaluation of str-ZPM Gel regeneration efficacy in vivo. a** Microscopic geomorphology at 8 weeks. **b** Young's modulus of different newborn cartilage tissues. Data were presented as the mean ± SD ($n = 3$ independent experiments). $^*P < 0.05$, $^{**}P < 0.01$, and $^{***}P < 0.001$. Statistical comparisons were performed using one-way ANOVA with Tukey's test. **c** Representative H&E, Toluidine blue and Safranin O/fast green staining at 8 weeks. Rectangular boxes on the left and right indicate new tissues and defect edges, respectively. **d** Heatmap of variables of histological scoring at 4 and 8 weeks. **e** Histological scores of different groups. Data were presented as the mean ± SD ($n = 4$ independent experiments). $^*P < 0.05$, $^{**}P < 0.01$, and $^{***}P < 0.001$. Statistical comparisons were performed using one-way ANOVA with Tukey's test. **f** Representative immunohistochemistry images showing the protein expression level of Aggrecan, COL2A1 and MMP13 at 4 and 8 weeks. **g**–**i** Quantitative analysis of immunohistochemical staining. Data were presented as the mean ± SD ($n = 4$ independent experiments). $^*P < 0.05$, $^{**}P < 0.01$, and $^{***}P < 0.001$. Statistical comparisons were performed using one-way ANOVA with Tukey's test. Source data are provided as a Source Data file.

signaling pathways[59]. However, the use of exogenous BMSCs has been hindered by ethical concerns and issues related to immune rejection[60]. Our study addressed this issue by leveraging endogenous BMSCs recruitment through str-ZPM Gel. We observed that the cells encapsulated in the 0.5% ZnO-doped GelMA hydrogel showed increased production of aggrecan and type II collagen, along with upregulated expression of cartilage markers. These findings suggest that the release of $Zn^{2+}$ contributes to the chondrogenic differentiation of stem cells. $Zn^{2+}$ is widely present in the bone matrix and promotes bone metabolism and regeneration[61,62], although the underlying molecular mechanisms of its biological activities remain unclear[21,63]. The str-ZPM Gel used in this study not only facilitated the sustained release of $Zn^{2+}$, but also provided a natural cartilage-like microenvironment, which further enhanced the induction of BMSCs differentiation.

Efficient delivery and sustained action of miR-17 at joint sites are crucial for inhibiting catabolism and enhancing therapeutic outcomes. Leveraging electrostatic interactions between a cationic delivery carrier and cartilage to enhance carrier retention has proven advantageous because of the abundance of negatively charged substances, such as proteoglycans, in cartilage tissue[64,65]. PEI is a well-studied cationic polymer for gene delivery, attributed to its robust DNA condensation and endosomolytic properties[66,67]. Although high molecular weight PEI (25 kDa) offers superior transfection efficiency owing to its dense cationic charge, it poses cytotoxicity concerns. Conversely, low molecular weight PEI (1.8 kDa) is less toxic, however, exhibits low transfection efficiency[68]. To optimize the performance, we loaded PEI (1.2 kDa) onto str-ZnO, capitalizing on cellular nanoparticle uptake to deliver nucleic acids into living cells effectively[69]. The rationale behind this lies in the notably heightened levels of transfection activity observed, demonstrating significantly enhanced efficiency with str-ZnO loaded with PEI/miR-17 compared to PEI/miR-17 alone. Overall, our study strongly suggests that the streamlined nanoparticles hold immense promise as potent enhancers of effective gene delivery.

Numerous studies have demonstrated that doping metal oxides into scaffolds can confer superior mechanical properties, making this an interesting area of exploration for ideal bone scaffolds[70–73]. For instance, Zhou et al. fabricated $Fe_2O_3$ nanoparticle-cross-linked GelMA hydrogels, revealing that increased $Fe_2O_3$ concentrations elevated hydrogel stiffness and augmented mitochondrial oxidative phosphorylation in chondrocytes, thereby boosting ATP production and cartilage regeneration[74]. Although their study highlights the potential of metal oxides to promote tissue repair via metabolic regulation, the use of a spherical nanoparticle morphology leaves the investigation of morphology-dependent dynamic material properties (e.g., shear-thinning behavior, injectability) open for further exploration. In contrast, our study systematically investigated how ZnO nanoparticle architecture governs hydrogel functionality. By comparing the morphologies of sph-ZnO and str-ZnO, we demonstrated that nanoparticle geometry critically determines both rheological behavior and gene delivery efficiency. Specifically, high-curvature str-ZnO exhibited a heightened tendency for rapid diffusion under the injection force, resulting in the formation of hydrogels with exceptional mechanical properties. We hypothesized that the distinctive streamlined configuration of str-ZnO contributed to the diminished resistance during injection, while affording a larger surface area for augmented interaction with the polymer chains within the hydrogel[75]. Viewed through a microscopic lens, the doped str-ZnO particles demonstrated the ability to form hydrogen bonds with neighboring polymer chains, fostering the establishment of a physically cross-linked network within the hydrogel system. These hydrogen bonds possess the capacity to absorb and dissipate external stress upon disruption. Notably, the superior specific surface area of str-ZnO compared to its spherical counterparts enables str-ZnO-loaded hydrogels to form a greater number of sacrificial hydrogen bonds, which can absorb elevated energy levels when subjected to external stimuli, thereby fortifying resistance against external shear damage. Throughout the injection process, the tailored str-ZnO exhibited low viscosity characteristics, which proved advantageous for improving the injectability and accommodating irregular tissue defects. Once the injection was completed, the hydrogel underwent an increase in in situ hardness, effectively preventing loss from the lesion site and establishing snug contact with the surrounding tissue. Importantly, the streamlined morphology of str-ZnO facilitated efficient penetration of the cell surface, meeting the requirements for achieving high gene transfection efficiency. This promising paradigm holds significant potential for future applications and advancements in gene therapy.

In summary, we developed a gene delivery system comprising three key components: an MMP-responsive hydrogel matrix, str-ZnO, and miR-17-5p. The responsive hydrogel served as a matrix to achieve a highly localized, sustained drug release triggered by MMPs. Str-ZnO acted as a gene transfection vector and facilitated chondrogenic differentiation of BMSCs by promoting the Ihh/PTHrP signaling pathway. MiR-17-5p counteracts ECM catabolism by targeting multiple catabolic factors, such as ADAMTS5, thereby inhibiting matrix-degrading enzymes. The synergistic effect of these three components balances ECM homeostasis by promoting anabolism and suppressing catabolism. This approach holds significant implications in the treatment of OA cartilage defects. Despite remarkable progress in cartilage tissue engineering, the creation of scaffolds or hydrogels with properties that can authentically emulate natural cartilage, facilitate cartilage regeneration, and bolster load-bearing capabilities, remains a persistent challenge. An extensive exploration of how stiffness influences cellular proliferation, differentiation, ECM production, and migration is imperative. Future investigations will concentrate on refining the formulation and cross-linking techniques of hydrogels to augment their overall efficacy and align them more closely with the characteristics of natural cartilage. Furthermore, relatively few ongoing clinical trials focus on injectable materials for cartilage repair. Furthermore, in vivo studies on the properties of hydrogels (e.g., controlled release and degradability) are urgently needed to improve their efficacy in large animal models and bring them closer to clinical therapeutic applications.

## Methods

### Materials

Anhydrous zinc acetate ($Zn(OAc)_2$ was obtained from Heowns Biotechnology Co., Ltd. (Tianjin, China). PEI (1.2 kDa), benzyl ether($(C_6H_5CH_2)_2O$), benzylamine ($C_6H_5CH_2NH_2$), and collagenase II were purchased from Sigma–Aldrich (St. Louis, MO, USA). Triton X-100, 1% BSA, and crystal violet were obtained from Yuanye Biotechnology Co., Ltd. (Shanghai, China). Gelatins, methacrylic anhydride (MA), and lithium phenyl-2,4,6 trimethylbenzoylphosphinate (LAP) were purchased from Aladdin Biochemical Technology Co., Ltd.

(Shanghai, China). DAPI was obtained from Solarbio Life Science and Technology Ltd. (Beijing, China). The Calcein/PI Cell Viability/Cytotoxicity Assay Kit and Immunol staining blocking buffer were obtained from Beyotime Biotechnology (Jiangsu, China). Primers used for q-PCR were purchased from Sangon Biotech Co., Ltd. (Shanghai, China). MiR-17-5p mimic, FAM-labeled MiR-17-5p mimic, MiR-17-5p inhibitor, Bulge-Loop™ miRNA qRT-PCR Primer, and riboFECT™CP Transfection were bought from RiboBio Co., Ltd. (Guangzhou, China). Cy3-labeled locked nucleic acid miR-17-5p probes were designed and synthesized by BersinBio-Technology Co., Ltd. (Guangzhou, China). The All-in-One First-Strand cDNA synthesis kit and Perfect Start Green q-PCR kit were obtained from Transgene Biotech, Inc. (Beijing, China). Rat IL-1β protein was bought from Abbkine Biotechnology Co., Ltd. (Wuhan, China). Rhodamine-WGA and TRITC-Phalloidin were purchased from Shanghai Maokang Biotechnology Co., Ltd. (Shanghai, China). Anti-collagen II, anti-ADAMTS5, anti-SOX9, and anti-Ihh antibodies were obtained from Abcam (Cambridge, UK). CD44 Polyclonal, CD90 Monoclonal, MMP13 polyclonal, aggrecan polyclonal, and PTHLH polyclonal antibodies were purchased from Proteintech Group, Inc. Cyclopamine was purchased from MedChemExpress (Shanghai, China). The zinc assay kit was bought from Nanjing Jiancheng Bioengineering Institute (Nanjing, China). All reagents used in this study were of the highest grade commercially available.

### Preparation of str-ZnO

Str-ZnO was synthesized based on previous studies with slight modifications[76]. Briefly, anhydrous $Zn(OAc)_2$ (1.83 g, 10 mmol) was dissolved in dibenzyl ether (100 mL) at a temperature of 210 °C. Subsequently, benzylamine (10.7 g, 100 mmol) was added to the reaction mixture, which underwent reflux for 5 h. After the completion of the reaction, the solution was cooled to room temperature, centrifuged and washed using acetone to obtain a white precipitate.

### Preparation of str-ZnO@PEI/miR-17 complexes

A suspension of 75 mg of str-ZnO in 15 mL of NaOH (0.1 M) solution was prepared under constant stirring for 5 min at room temperature. Subsequently, 7.5 mL of epichlorohydrin and 0.75 mL of NaOH (2 M) were added to the suspension, which was stirred at room temperature for 8 h. After this period, the reaction mixture was washed using deionized water (two or three times) and centrifuged at 7040 ×g for 5 min to obtain epichlorohydrin-coated str-ZnO. Subsequently, a molar ratio of 10:1 epichlorohydrin-coated str-ZnO with PEI was stirred at room temperature for 24 h. Branched-PEI 1.2 kDa initiated the opening of the epoxide ring on the epichlorohydrin molecule, resulting in the formation of str-ZnO@PEI ($SN_2$ reaction) (Supplementary Fig. 1b)[77]. Next, the reaction mixture was washed two or three times with deionised water and centrifuged at 1126×*g* for 10 min to obtain str-ZnO@PEI. The str-ZnO@PEI/miR-17 complexes were induced by adding miR-17-5p mimic solution to the str-ZnO@PEI solution at a mass ratio of 1:5 and incubating the combination at 4 °C for 30 min. All the complexes were freshly prepared before use.

### Synthesis of GelMA/str-ZnO composite hydrogels and str-ZPM Gel

In this procedure, 10% GelMA was synthesized by adding gelatin and MA. Briefly, 10 g of gelatin was completely dissolved in PBS at a mass fraction of 10% in a water bath set at 50 °C. Subsequently, 5 mL of MA was slowly added to the solution with vigorous stirring for 2 h. Following completion of the reaction, the solution was filtered and transferred into a dialysis bag with a molecular weight of 3500. The solution was then dialyzed for 5 days at 40° to eliminate unreacted MA. Upon the completion of the dialysis process, the GelMA precursor, which appeared as a white foam, was obtained by freeze-drying. The pre-gel solution was prepared by dissolving 10% GelMA, 0.3% LAP, and various ZnO mass fractions in deionized water with sufficient stirring. Finally, this solution was exposed to 405 nm UV light for 60 s to generate GelMA/str-ZnO composite hydrogels. In the formation of str-ZPM Gel, 0.5 mg miR-17 was preloaded onto str-ZnO@PEI at a mass ratio of 1:5 to form str-ZnO@PEI/miR-17 complexes. The complexes were then dispersed in 0.5 mL of PBS buffer solution (pH 7.4) containing 50 mg/0.5 mL of GelMA and 1.5 mg/0.5 mL of LAP. The mixture was then incubated at room temperature for 10 min and cross-linked using UV radiation for 60 s.

### Agarose gel assay for the formation of str-ZnO@PEI/miR-17 complexes

str-ZnO@PEI/miR-17 complexes were prepared at different weight ratios (0, 1, 5, 10, and 15) and subsequently diluted with water to a final volume of 20 μL. The complexes were vortexed and incubated at room temperature for 30 min. Following incubation, the supernatants were subjected to electrophoresis on a 0.8% (w/v) agarose gel at 100 V for 30 min. RNA bands were visualized and captured using an Image-master VDS thermal imaging system (Bio-Rad, Hercules, CA, USA).

### In vivo hydrogel degradation analysis

The str-ZPM Gel was transplanted into the site of cartilage defects in rats. Photographs were taken on days 1, 28, and 36 after surgery (AniView100, China) using a cy5 channel (excitation: 605 nm, emission: 680 nm). The total radiance (p/s/cm$^2$/sr) of the samples was obtained using live imaging software to analyze the biodegradation trend curve of the str-ZPM Gel.

### Viscosity and injectable properties characterization

The rheological characterization and stress recovery analysis of the composite hydrogels were performed using a rheometer (DHR-2, Waters™ TA Instruments, USA). The shear stresses of the hydrogel samples, varying with the ZnO content (0, 0.5, 1, and 2%), were measured at room temperature with a shear rate range of 0.1–100 s$^{-1}$. For the stress recovery test, the composite hydrogels were subjected to consecutive high- (200%, 60 s) and low-strain (1%, 60 s) cycles at a frequency of 1 Hz. This allowed the determination of the storage modulus (G′) and loss modulus (G″) of the composite hydrogels. The injectability of the composite hydrogels was assessed using a needle syringe at room temperature.

### Locomotion experiments

To assess the movement of nanoparticles in solutions containing GelMA, we analyzed the trajectories of individual nanoparticles by NTA using a Nanosight NS300 device (Malvern, UK). Samples were diluted in PBS buffer and introduced into the Nanosight chamber at 25 °C with a syringe pump pressure of 100 μL/min. The motion of the nanoparticles was recorded as videos for 60 s at a speed of 25 frames s$^{-1}$. NTA 3.4 software was used to track the $x$ and $y$ trajectories of the nanoparticles, and their mean square displacement (MSD) was calculated[78].

### Mechanical tests

Cylindrical hydrogel samples, 30 mm in diameter and 4 mm in height, were fabricated through UV light cross-linking. Compression testing of the samples was performed at a rate of 1 mm/min at a temperature of 25 °C using an electronic universal testing machine (AGS-X, Shimadzu, Japan) until the instrument loading limit was stopped. The first 0–10% linear region of the stress-strain curve was calculated to obtain the elastic modulus of the sample.

### In vitro hydrogel degradation

To evaluate the degradation behavior of hydrogels with varying ZnO contents (0, 0.5, 1, and 2%), the samples (30 mm in diameter and 4 mm in height) were immersed in an aqueous solution of collagenase II (100 μg/mL) at 37 °C. The enzyme-containing solution was replaced

every 3 days to ensure the presence of active collagenase. At specific time intervals (days 1, 3, 5, 7, 10, 14, 21, 28, 35, and 42), the mass of the hydrogel was measured after removal of the surface supernatant. The primary mass of the gel was denoted as $W_0$, whereas the hydrogel mass at a specific time point was recorded as $W_t$. Degradation rate (%) = $W_t/W_O \times 100\%$.

### str-ZnO@PEI/miR-17 complex release detection

The hydrogel was formed as described above, with the only difference being the use of using FITC-labeled str-ZnO@PEI/miR-17 instead of pure str-ZnO@PEI/miR-17. Briefly, the hydrogel formed in the upper layer of the transwell was immersed in a 12-well plate filled with 1 mL of PBS or collagenase II (100 μg/mL) solution at 37 °C, respectively. At predetermined time intervals, the suspension was removed and replaced with fresh, prewarmed PBS or collagenase II. The suspensions were measured using a microplate reader (FlexStation 3, USA) to determine the release of the str-ZnO@PEI/miR-17 complex from the hydrogel into the buffer solution.

### miR-17-5p release detection

The release profile of miR-17 from the str-ZnO@PEI/miR-17 complexes was examined in 0.1 M PBS at two different pH values (pH 7.4, pH 5.0). The concentration of miR-17 in the solution after incubation at 37 °C for various time points was measured using Nanodrop (Thermo Fisher Scientific, Waltham, MA, USA).

### Cell viability and proliferation assay

The proliferation of BMSCs (Procell, CP-R131) and chondrocytes (Procell, CP-R087) stimulated by the hydrogel was detected using a Calcein/PI Cell Viability/Cytotoxicity Assay Kit. Briefly, cells were seeded in 12-well transwell plates at a density of $2 \times 10^5$ cells per well. After incubation with the str-ZPM Gel for 1, 3, and 5 days, the upper chamber was removed, and the cells were washed twice with PBS. According to the manufacturer's protocol, 500 μL of the prepared live/dead cell staining solution was added to each well to stain the cells. Subsequently, cells were incubated for 30 min at 37 °C protected from light before washing with PBS and visualized by laser confocal microscopy (Leica SP 8, Germany).

For the toxicity assay, aseptically processed gels with a total volume of 50 μl were prepared in 96-well plates and seeded with $1 \times 10^4$ cells. After 1, 3, and 5 days of coculture, the original medium was discarded, and medium containing 10% CCK-8 was added and incubated for 1 h. The 100 μl supernatant from each well was then transferred to a new 96-well plate and read at 450 nm using a microplate reader (FlexStation 3, USA).

### In vitro cell uptake of sph-ZnO and str-ZnO

FITC-labeled streamlined and spherical ZnO was incubated with the BMSCs for 15 min at 37 °C. After incubation, the samples were washed with PBS, fixed with 4% paraformaldehyde for 10 min, and washed again with PBS. Cellular membranes were stained with Rhodamine-WGA (5 μg/mL) at room temperature for 10 min. The nuclei were then stained with DAPI and observed using a confocal laser scanning microscope (Leica SP 8, Germany).

### Cytoskeleton staining

To investigate the biocompatibility of the composite hydrogel, cytoskeletal staining was performed to observe the adhesion behavior of the cells on the hydrogel after culturing rat chondrocytes and BMSCs for 2 days. The medium was removed, the cells were gently washed three times with PBS, and fixed with 4% paraformaldehyde for 10 min. After washing, the cells were permeabilized with 0.1% Triton X-100 in PBS for 5 min and subsequently blocked with 1% BSA for 5 min. After removing the liquid, cells were stained with freshly prepared TRITC-phalloidin for 30 min at room temperature and then washed with PBS. The nuclei were stained with DAPI and observed using a confocal laser scanning microscope (Leica SP 8, Germany). The cell spreading area was quantified using the ImageJ software (National Institute of Health, USA).

### RNA fluorescent in situ hybridization (FISH)

Cy3-labeled locked nucleic acid miR-17-5p probes were designed and synthesized by BersinBio-Technology Co., Ltd. (Guangzhou, China). Probe signals were detected using a fluorescent in situ hybridization kit (BersinBio), according to the manufacturer's instructions. For in vivo FISH, tissue sections were deparaffinized, dehydrated, and permeabilized using proteinase K treatment (37 °C for 15 min) before hybridization. The cells were then stained with DAPI for 10 min, washed with PBS, and observed using an automatic slide scanning system.

### Immunofluorescence (IF)

The chondrocytes and BMSCs were fixed with 4% paraformaldehyde for 10 min and permeabilized with 0.1% Triton X-100 for 5 min, followed by blocking with Immunol staining blocking buffer for 1 h at 25 °C. The cells were then incubated overnight at 4 °C with anti-SOX9 (1:250, ab185966, Abcam). Then, the cells were incubated with TRITC-phalloidin for 30 min and goat anti-rabbit IgG H&L (Alexa Fluor 488, 1:200, ab150081, Abcam) for 1 h at 25 °C. Nuclei were stained with DAPI, and the cells were imaged using laser confocal microscopy (Leica SP 8, Germany).

### Migration of BMSCs in vitro

In this study, 200 μL of BMSCs suspension ($1 \times 10^5$ cells/mL) was inoculated into the upper layer of the Transwell in a 24-well plate. Then, 0.5 mL of α-MEM medium (containing 10% fetal bovine serum) was added to the lower chamber and incubated for 12 h. Subsequently, composite hydrogel samples were loaded in the lower chamber for 12 h incubation and the medium were replaced with serum-free medium. The chambers were removed to absorb excess liquid and washed three times with PBS. The cells were fixed in 4% paraformaldehyde for 20 min, washed with PBS, and stained with 0.1% crystal violet for 10 min. After gentle rinsing with PBS, migrated cells were photographed using a light microscope and counted.

### Chondrogenic differentiation induction in BMSC

Rat BMSCs were seeded in the lower chamber of a 6-well plate at a density of $1 \times 10^5$ / well, while the hydrogel was placed in the upper chamber. The induction medium was replaced after 24 h (material-free medium system served as the control group). After 7 or 21 days of culture in the hydrogel, the expression of typical chondrogenic (SOX9, COL2A1, and Aggrecan) and catabolic genes (MMPl3 and ADAMTS5) was detected using RT-PCR. The primer sequences are listed in Table S1.

### Western blotting analysis

Proteins from the cell lysates were separated by 4–10% SDS-polyacrylamide gel electrophoresis (SDS-PAGE) and transferred onto a polyvinylidene fluoride membrane. The membranes were blocked with 5% dry milk–TBST for 1 h and incubated with anti-β-tubulin (1:2000, TA-10, ZSGB-BIO), anti-PTHLH (1:500, 10817-1-AP, Proteintech), anti-Ihh (1:5000, ab52919, Abcam), anti-MMP13 (1:500; 18165-1-AP, Proteintech), anti-ADAMTS5 (1:250, ab41037, Abcam), anti-Aggrecan (1:1000, 13880-1-AP, Proteintech), anti-SOX9 (1:5000, ab185966, Abcam), and anti- Collagen II antibodies (1:4000, ab34712, Abcam) at 4 °C overnight, respectively. The membranes were washed thoroughly with TBST and incubated for 1 h at room temperature with horse radish peroxidase (HRP)-conjugated Goat Anti-Rabbit IgG (1:5000, ZB-2301, ZSGB-BIO) and HRP-conjugated Goat Anti-Mouse IgG (1:5000, ZB-2305, ZSGB-BIO). Antibody reactivity was visualized

using a fully automated chemiluminescence/gel imaging system (Champchemi 610 Plus, China) and quantified using ImageJ software.

### Transcriptomic analysis

In this study, $5 \times 10^6$/well BMSCs were cultured with the Control, PEI/miR-17, and str-ZPM Gel groups for 7 days. Three biological replicates were collected from each experimental group and snap-frozen in liquid nitrogen. The RNA was sequenced by Sangon Biotech Co., Ltd. (Shanghai, China).

### Rat model of OA

Male Sprague Dawley rats (7 weeks old) were obtained from HFK Bio-Technology Co., Ltd. (Beijing, China) and housed in a controlled environment with regulated temperature and humidity for 1 week of acclimation. Rats were housed under the ambient temperature of 25 ± 2 °C, circulating air, constant humidity of 60 ± 10%, and a 12 h:12 h light/dark cycle. All animal procedures were performed according to the guidelines for the Care and Use of Laboratory Animal Experience of Tianjin University and approved by the Animal Ethics Committee of Tianjin University (license number: SYXK (Jin) 2019-0002). Male rats were selected because the estrogen levels in female rats influence the development of OA. To establish a typical OA cartilage defect, an incision was made on the lateral side of the patella to expose the articular cartilage of the distal femur on the face of the kneecap. Subsequently, a cylindrical defect ~2 mm in diameter and 1.5 mm in depth was operated with a manual drill to construct a defect model involving the entire cartilage layer. The SD rats were randomly divided into four groups: (1) sham, (2) OCD (modeling group), (3) str-ZP Gel (GelMA/str-ZnO@PEI/miR-NC), and (4) str-ZPM Gel. For Groups 3 and 4, cartilage defects were created to implant the experimental hydrogels into the defect, followed by layer-by-layer suturing after flushing the incision with normal saline. The experimental animals were kept in cages and allowed to move freely.

### Micro–computed tomography (Micro-CT)

Four weeks after surgery, the rats were euthanized, and knee joint samples were subjected to micro-CT imaging (Quantum FX, PerkinElmer, USA). Briefly, an X-ray energy of 90 kV and a 4.5 min exposure time were used to image the knee articular cartilage, distal femur, and proximal tibia. According to the results of the micro-CT scanning and reconstruction, BMD, BV/TV, Tb. N, Tb. Th, and Tb. Sp were analyzed.

### Tissue zinc ion content assessment

The tissue samples were weighed and homogenates were prepared in an ice-water bath according to a ratio of 40 mg tissue to 360 µL of PBS. The homogenate was centrifuged at 1500 × *g* for 10 min at 4 °C, and the supernatant was collected for testing. The absorbance at 630 nm was recorded using a microplate spectrophotometer to calculate the concentration of Zn according to the manufacturer's instructions.

### Biomechanical assessment

Eight weeks post-surgery, a biomechanical assessment of the repaired cartilage area was conducted utilizing a NanoWizard4 BioScience atomic force microscope (JPK, Germany) on samples of frozen sections with a thickness of 10 µm. The elastic modulus and cartilage morphology were quantified using a tesp-v2 probe with a 7 nm radius of curvature.

### Histological and immunohistochemical analysis

Knee cartilage specimens from rats at the 4th and 8th week after execution were fixed, decalcified with 4% paraformaldehyde, and embedded in paraffin. The specimens were cut into 4-µm-thick sections (HistoCore MULTICUT, China) to respectively perform safranin o/fast green, toluidine blue, hematoxylin-eosin (H&E), and immunohistochemical staining after deparaffinization and hydration. The sections were imaged using a pathological panoramic scanner (3DHISTECH P250 FLASH, China).

### Score system to evaluate the degree of cartilage regeneration

Independent professionals with knowledge and experience in cartilage histology independently performed the morphological evaluations of cartilage regeneration. The evaluation was based on the ICRS macroscopic evaluation of the cartilage and the ICRS visual histological assessment scale[48].

### Statistical analysis

Statistical significance between two groups was assessed using an unpaired two-sided Student's *t*-test. One-way analysis of variance (ANOVA) was used for multigroup comparisons. All data in this study were statistically analyzed by GraphPad Prism software (version 9.0, GraphPad Software Inc., USA) and shown as mean ± standard deviation (SD). $P < 0.05$ was considered statistically significant. No statistical methods were used to predetermine the sample size. No data were excluded from the analyses. The experiments were randomized. The investigators were blinded to the allocation during the experiments and outcome assessment.

### Reporting summary

Further information on research design is available in the Nature Portfolio Reporting Summary linked to this article.

## Data availability

All data were available in the main text or the supplementary materials. The RNA sequencing data generated in this study were deposited in the NCBI Sequence Read Archive database under the accession number PRJNA1242216. Source data are provided with this paper.

## References

1. Yang, Y. et al. Controlled release of MSC-derived small extracellular vesicles by an injectable Diels-Alder crosslinked hyaluronic acid/PEG hydrogel for osteoarthritis improvement. *Acta Biomater.* **128**, 163–174 (2021).
2. Abramoff, B. & Caldera, F. E. Osteoarthritis: pathology, diagnosis, and treatment options. *Med. Clin. North. Am.* **104**, 293–311 (2020).
3. Martel-Pelletier, J. et al. Osteoarthritis. *Nat. Rev. Dis. Prim.* **2**, 16072 (2016).
4. Yang, Z. et al. Endogenous cell recruitment strategy for articular cartilage regeneration. *Acta Biomater.* **114**, 31–52 (2020).
5. Wang, K.-Y. et al. Injectable stress relaxation gelatin-based hydrogels with positive surface charge for adsorption of aggrecan and facile cartilage tissue regeneration. *J. Nanobiotechnol.* **19**, 214 (2021).
6. Zhu, J. et al. Stem cell–homing hydrogel-based miR-29b-5p delivery promotes cartilage regeneration by suppressing senescence in an osteoarthritis rat model. *Sci. Adv.* **8**, eabk0011 (2022).
7. Howell, M., Liao, Q. & Gee, C. W. Surgical management of osteochondral defects of the knee: an educational review. *Curr. Rev. Musculoskelet. Med.* **14**, 60–66 (2021).
8. Hardingham, T. E. & Fosang, A. J. Proteoglycans: many forms and many functions. *FASEB J.* **6**, 861–870 (1992).
9. Zheng, L., Zhang, Z., Sheng, P. & Mobasheri, A. The role of metabolism in chondrocyte dysfunction and the progression of osteoarthritis. *Ageing Res. Rev.* **66**, 101249 (2021).
10. Poulet, B. & Staines, K. A. New developments in osteoarthritis and cartilage biology. *Curr. Opin. Pharmacol.* **28**, 8–13 (2016).

11. Dong, Y. et al. Spatiotemporal regulation of endogenous MSCs using a functional injectable hydrogel system for cartilage regeneration. *NPG Asia Mater.* **13**, 71 (2021).
12. Liu, Y. et al. Spatiotemporal immunomodulation using biomimetic scaffold promotes endochondral ossification-mediated bone healing. *Adv. Sci.* **8**, 2100143 (2021).
13. Feng, L. et al. MicroRNA-378 contributes to osteoarthritis by regulating chondrocyte autophagy and bone marrow mesenchymal stem cell chondrogenesis. *Mol. Ther. Nucleic Acids* **28**, 328–341 (2022).
14. Chen, G., Deng, C. & Li, Y.-P. TGF-β and BMP signaling in osteoblast differentiation and bone formation. *Int. J. Biol. Sci.* **8**, 272–288 (2012).
15. Roelen, B. A. J. & Dijke, P. T. Controlling mesenchymal stem cell differentiation by TGFβ family members. *J. Orthop. Sci.* **8**, 740–748 (2003).
16. Schmidt, M. B., Chen, E. H. & Lynch, S. E. A review of the effects of insulin-like growth factor and platelet derived growth factor on in vivo cartilage healing and repair. *Osteoarthr. Cartil.* **14**, 403–412 (2006).
17. Kawai, M. et al. Non-surgical model for alveolar bone regeneration by bone morphogenetic protein-2/7 gene therapy. *J. Periodontol.* **89**, 85–92 (2018).
18. Read, S. A., Obeid, S., Ahlenstiel, C. & Ahlenstiel, G. The role of zinc in antiviral immunity. *Adv. Nutr.* **10**, 696–710 (2019).
19. Narayanan, S. E. et al. Molecular mechanism of zinc neurotoxicity in Alzheimer's disease. *Environ. Sci. Pollut. Res.* **27**, 43542–43552 (2020).
20. Perez, R. A. et al. Therapeutically relevant aspects in bone repair and regeneration. *Mater. Today* **18**, 573–589 (2015).
21. Chen, Z., Zhang, W., Wang, M., Backman, L. J. & Chen, J. Effects of zinc, magnesium, and iron ions on bone tissue engineering. *ACS Biomater. Sci. Eng.* **8**, 2321–2335 (2022).
22. Fielding, G. & Bose, S. SiO2 and ZnO dopants in three-dimensionally printed tricalcium phosphate bone tissue engineering scaffolds enhance osteogenesis and angiogenesis in vivo. *Acta Biomater.* **9**, 9137–9148 (2013).
23. Fielding, G. A., Bandyopadhyay, A. & Bose, S. Effects of silica and zinc oxide doping on mechanical and biological properties of 3D printed tricalcium phosphate tissue engineering scaffolds. *Dent. Mater.* **28**, 113–122 (2012).
24. Krzeski, P. et al. Development of musculoskeletal toxicity without clear benefit after administration of PG-116800, a matrix metalloproteinase inhibitor, to patients with knee osteoarthritis: a randomized, 12-month, double-blind, placebo-controlled study. *Arthritis Res. Ther.* **9**, R109 (2007).
25. Li, X. et al. The protective effect of ligustilide in osteoarthritis: an in vitro and in vivo study. *Cell. Physiol. Biochem.* **48**, 2583–2595 (2018).
26. Paunovska, K., Loughrey, D. & Dahlman, J. E. Drug delivery systems for RNA therapeutics. *Nat. Rev. Genet.* **23**, 265–280 (2022).
27. Ventura, A. et al. Targeted deletion reveals essential and overlapping functions of the miR-17~92 family of miRNA clusters. *Cell* **132**, 875–886 (2008).
28. Zhang, Y. et al. Dual functions of microRNA-17 in maintaining cartilage homeostasis and protection against osteoarthritis. *Nat. Commun.* **13**, 2447 (2022).
29. Walters, N. J. & Gentleman, E. Evolving insights in cell–matrix interactions: elucidating how non-soluble properties of the extracellular niche direct stem cell fate. *Acta Biomater.* **11**, 3–16 (2015).
30. Pan, Y. & Xiong, D. Study on compressive mechanical properties of nanohydroxyapatite reinforced poly(vinyl alcohol) gel composites as biomaterial. *J. Mater. Sci. Mater. Med.* **20**, 1291–1297 (2009).
31. Zaragoza, J., Fukuoka, S., Kraus, M., Thomin, J. & Asuri, P. Exploring the role of nanoparticles in enhancing mechanical properties of hydrogel nanocomposites. *Nanomaterials* **8**, 882 (2018).
32. Baek, K., Shin, H., Yoo, T. & Cho, M. Two-step multiscale homogenization for mechanical behaviour of polymeric nanocomposites with nanoparticulate agglomerations. *Compos. Sci. Technol.* **179**, 97–105 (2019).
33. Chang, A., Babhadiashar, N., Barrett-Catton, E. & Asuri, P. Role of nanoparticle–polymer interactions on the development of double-network hydrogel nanocomposites with high mechanical strength. *Polymers* **12**, 470 (2020).
34. Albanese, A., Tang, P. S. & Chan, W. C. W. The effect of nanoparticle size, shape, and surface chemistry on biological systems. *Annu. Rev. Biomed. Eng.* **14**, 1–16 (2012).
35. Geng, Y. et al. Shape effects of filaments versus spherical particles in flow and drug delivery. *Nat. Nanotechnol.* **2**, 249–255 (2007).
36. Dasgupta, S., Auth, T. & Gompper, G. Shape and orientation matter for the cellular uptake of nonspherical particles. *Nano Lett.* **14**, 687–693 (2014).
37. Li, J. et al. Targeting endogenous hydrogen peroxide at bone defects promotes bone repair. *Adv. Funct. Mater.* **32**, 2111208 (2022).
38. Jiang, X. et al. Curvature-mediated rapid extravasation and penetration of nanoparticles against interstitial fluid pressure for improved drug delivery. *Proc. Natl Acad. Sci. USA* **121**, e2319880121 (2024).
39. Chimene, D., Kaunas, R. & Gaharwar, A. K. Hydrogel bioink reinforcement for additive manufacturing: a focused review of emerging strategies. *Adv. Mater.* **32**, 1902026 (2020).
40. Yang, J., Han, C.-R., Duan, J.-F., Xu, F. & Sun, R.-C. Mechanical and viscoelastic properties of cellulose nanocrystals reinforced poly(ethylene glycol) nanocomposite hydrogels. *ACS Appl. Mater. Interfaces* **5**, 3199–3207 (2013).
41. Kim, K.-J. et al. Magnesium ions enhance infiltration of osteoblasts in scaffolds via increasing cell motility. *J. Mater. Sci. Mater. Med.* **28**, 96 (2017).
42. Yu, Y. et al. Multifunctions of dual Zn/Mg ion co-implanted titanium on osteogenesis, angiogenesis and bacteria inhibition for dental implants. *Acta Biomater.* **49**, 590–603 (2017).
43. Kamper, M., Paulsson, M. & Zaucke, F. Absence of collagen IX accelerates hypertrophic differentiation in the embryonic mouse spine through a disturbance of the Ihh-PTHrP feedback loop. *Cell Tissue Res.* **367**, 359–367 (2017).
44. Cai, H. & Liu, A. Spop promotes skeletal development and homeostasis by positively regulating Ihh signaling. *Proc. Natl Acad. Sci. USA* **113**, 14751–14756 (2016).
45. Taipale, J. et al. Effects of oncogenic mutations in Smoothened and Patched can be reversed by cyclopamine. *Nature* **406**, 1005–1009 (2000).
46. Nybakken, K. & Perrimon, N. Hedgehog signal transduction: recent findings. *Curr. Opin. Genet. Dev.* **12**, 503–511 (2002).
47. Li, J. et al. Articular fibrocartilage-targeted therapy by microtubule stabilization. *Sci. Adv.* **8**, eabn8420 (2022).
48. Sun, X. et al. In situ articular cartilage regeneration through endogenous reparative cell homing using a functional bone marrow-specific scaffolding system. *ACS Appl. Mater. Interfaces* **10**, 38715–38728 (2018).
49. Jiang, S. et al. Mirror movements induced by hemiballism due to putamen infarction: a case report and literature review. *Ann Transl Med.* **8**, 19 (2019).
50. Peng, Z. et al. The regulation of cartilage extracellular matrix homeostasis in joint cartilage degeneration and regeneration. *Biomaterials* **268**, 120555 (2021).

51. Stanton, H. et al. ADAMTS5 is the major aggrecanase in mouse cartilage in vivo and in vitro. *Nature* **434**, 648–652 (2005).
52. Rose, B. J. & Kooyman, D. L. A tale of two joints: the role of matrix metalloproteases in cartilage biology. *Dis. Markers* **2016**, 4895050 (2016).
53. Goldring, M. B. Update on the biology of the chondrocyte and new approaches to treating cartilage diseases. *Best. Pract. Res. Clin. Rheumatol.* **20**, 1003–1025 (2006).
54. Goldring, M. B. The role of the chondrocyte in osteoarthritis. *Arthritis Rheum.* **43**, 1916-1926 (2000).
55. Kühn, K., D'Lima, D. D., Hashimoto, S. & Lotz, M. Cell death in cartilage. *Osteoarthr. Cartil.* **12**, 1–16 (2004).
56. Zhang, S. et al. Remodeling articular immune homeostasis with an efferocytosis-informed nanoimitator mitigates rheumatoid arthritis in mice. *Nat. Commun.* **14**, 817 (2023).
57. Liu, Y. et al. 3D-bioprinted BMSC-laden biomimetic multiphasic scaffolds for efficient repair of osteochondral defects in an osteoarthritic rat model. *Biomaterials* **279**, 121216 (2021).
58. Zhao, Y. et al. Nanozyme-reinforced hydrogel as a $H_2O_2$-driven oxygenerator for enhancing prosthetic interface osseointegration in rheumatoid arthritis therapy. *Nat. Commun.* **13**, 6758 (2022).
59. Ha, M. Y., Yang, D. H., You, S. J., Kim, H. J. & Chun, H. J. In-situ forming injectable GFOGER-conjugated BMSCs-laden hydrogels for osteochondral regeneration. *npj Regen. Med.* **8**, 2 (2023).
60. Park, Y.-B., Ha, C.-W., Lee, C.-H., Yoon, Y. C. & Park, Y.-G. Cartilage regeneration in osteoarthritic patients by a composite of allogeneic umbilical cord blood-derived mesenchymal stem cells and hyaluronate hydrogel: results from a clinical trial for safety and proof-of-concept with 7 years of extended follow-up. *Stem Cell Transl. Med.* **6**, 613–621 (2016).
61. Fu, X. et al. Runx2/Osterix and zinc uptake synergize to orchestrate osteogenic differentiation and citrate containing bone apatite formation. *Adv. Sci.* **5**, 1700755 (2018).
62. Zreiqat, H. et al. The incorporation of strontium and zinc into a calcium–silicon ceramic for bone tissue engineering. *Biomaterials* **31**, 3175–3184 (2010).
63. Kazimierczak, P., Kolmas, J. & Przekora, A. Biological response to macroporous chitosan-agarose bone scaffolds comprising Mg- and Zn-doped nano-hydroxyapatite. *Int. J. Mol. Sci.* **20**, 3835 (2019).
64. Sophia Fox, A. J., Bedi, A. & Rodeo, S. A. The basic science of articular cartilage: structure, composition, and function. *Sports Health* **1**, 461–468 (2009).
65. Vedadghavami, A. et al. Cartilage penetrating cationic peptide carriers for applications in drug delivery to avascular negatively charged tissues. *Acta Biomater.* **93**, 258–269 (2019).
66. Neuberg, P. & Kichler, A. in *Advances in Genetics* (eds. Huang L., Liu D. & Wagner E.) (Academic Press, 2014).
67. Lungwitz, U., Breunig, M., Blunk, T. & Göpferich, A. Polyethylenimine-based non-viral gene delivery systems. *Eur. J. Pharm. Biopharm.* **60**, 247–266 (2005).
68. Kunath, K. et al. Low-molecular-weight polyethylenimine as a non-viral vector for DNA delivery: comparison of physicochemical properties, transfection efficiency and in vivo distribution with high-molecular-weight polyethylenimine. *J. Control. Release* **89**, 113–125 (2003).
69. Sokolova, V. & Epple, M. Inorganic nanoparticles as carriers of nucleic acids into cells. *Angew. Chem. Int. Ed. Engl.* **47**, 1382–1395 (2008).
70. Gang, F. et al. Thermochemotherapy meets tissue engineering for rheumatoid arthritis treatment. *Adv. Funct. Mater.* **31**, 2104131 (2021).
71. Zhou, H. et al. A three-in-one strategy: injectable biomimetic porous hydrogels for accelerating bone regeneration via shape-adaptable scaffolds, controllable magnesium ion release, and enhanced osteogenic differentiation. *Biomacromolecules* **22**, 4552–4568 (2021).
72. Siebert, L. et al. Light-controlled growth factors release on tetrapodal ZnO-incorporated 3D-printed hydrogels for developing smart wound scaffold. *Adv. Funct. Mater.* **31**, 2007555 (2021).
73. Wang, X. et al. Recent strategies and advances in hydrogel-based delivery platforms for bone regeneration. *Nanomicro Lett.* **17**, 73 (2024).
74. Zhou, C. et al. Hydrogel platform with tunable stiffness based on magnetic nanoparticles cross-linked GelMA for cartilage regeneration and its intrinsic biomechanism. *Bioact. Mater.* **25**, 615–628 (2023).
75. Meng, X. et al. Hysteresis-free nanoparticle-reinforced hydrogels. *Adv. Mater.* **34**, 2108243 (2022).
76. De Corrado, J. M. et al. ZnO colloid crystal facet-type determines both Au photodeposition and photocatalytic activity. *ACS Appl. Nano Mater.* **2**, 7856–7869 (2019).
77. Patil, S., Reshetnikov, S., Haldar, M. K., Seal, S. & Mallik, S. Surface-derivatized nanoceria with human carbonic anhydrase II inhibitors and fluorophores: a potential drug delivery device. *J. Phys. Chem. C.* **111**, 8437–8442 (2007).
78. Díez, P. et al. Ultrafast directional Janus Pt–mesoporous silica nanomotors for smart drug delivery. *ACS Nano* **15**, 4467–4480 (2021).


## Acknowledgements

This study was supported by the National Natural Science of China (No. 82273873) (N.L.), Young Scientists Fund of the National Natural Science Foundation of China (No. 22305173) (Z.S.), Tianjin Natural Science Foundation (No. 21JCYBJC00660) (N.L.), and the Tianjin Graduate Student Research Innovation Program (No. 2022BKYZ011) (W.L.).

## Author contributions

N.L. supervised and revised the manuscript. W.L. synthesized the materials, completed the in vitro and in vivo experiments, and wrote the original draft. Z.S. and Z.H. assisted in revising the manuscript. H.J., Y.D., and X.L. assisted with the in vitro and in vivo experiments. M.Z. and Z.Q. provided advice for the cell experiments.

## Competing interests

The authors declare no competing interests.

## Additional information

**Supplementary information** The online version contains supplementary material available at https://doi.org/10.1038/s41467-025-59725-y.

**Correspondence** and requests for materials should be addressed to Nan Li.

**Peer review information** *Nature Communications* thanks Yi Cao who co-reviewed with Bin XueLei Cui, Cunyi Fan and the other, anonymous, reviewers for their contribution to the peer review of this work. A peer review file is available.